7. Non-adaptive wavefront control

7.1 Requirements

One of the objectives of OWL is diffraction limited imaging at all wavelengths. This is only possible with a concerted control of all optical elements correcting both the wavefront errors introduced by the optical elements themselves and those introduced by the atmosphere. Traditionally the control mechanisms are classified according to the origins of the wavefront errors, their frequency content, and their ranges of correction.

- **Pre-alignment.**

  At the end of the integration of the telescope (or after major maintenance operations) the optical elements are both misaligned with respect to each other and intrinsically deformed to such an extent that automatic measurements of the wavefront errors would fail. At this stage one needs a coarse alignment to reach the accuracies required for automatic correction procedures[58].

- **Active optics.**

  Active optics is defined as the correction of all errors which are generated by misalignments and deformations of the optical elements at frequencies lower than 0.1 Hz

- **Phasing of segmented mirrors.**

  The phasing of the two segmented mirrors is done at three levels. At the highest level, with optical measurements done at the beginning of the night, it can be regarded as a part of the active optics system. The global shapes of the segmented mirrors are corrected and, as a by-product, reference values for the edge sensors at the segment borders are defined. At the second level the corrections are based entirely on the measurements of the piston steps by the edge sensors at a rate of a few Hertz. While the highest two levels apply coupled corrections of the positions of the segments, the third level corrects the positions of single segments only, relying on measurements of parameters like accellarations of individual segments. This lowest stage may be required for the correction of wind effects at frequencies above 3 Hz.

- **Guiding and field stabilisation.**

  The control of the image position is done in two frequency regimes based on signals from a guiding camera. At low temporal frequencies up to the order of 1 Hz, guiding corrects the image position by controlling the azimuth and altitude positions of the telescope structure. At frequencies up to 10Hz, field stabilisation corrects residual errors in the image position

---

[58] In practice we expect the pre-alignment loop to run permanently (at very low frequency) in order to ensure that the system is always in a state allowing fast and linear convergence of the subsequent control loops.

with M6, either by rigid body movements of the support of M6 or by an overall tilt introduced into the thin adaptive mirror.

- **Atmospheric dispersion correction**

  Corrections to the level of a few milliarcseconds can most likely only be achieved with a closed-loop system estimating the residual chromatic aberrations due to the atmosphere. This requires a dedicated sensor measuring the positions of images obtained with light at two or more different narrow wavelength bands.

- **Adaptive Optics**

  Adaptive optics, which will be described in a separate chapter, is capable of correcting, at least partially, all types of wavefront errors by appropriate optical elements in the optical train. These can be either part of the telescope optics or of the instruments. Adaptive optics relies on signals obtained with high sampling rates of the order of up to a few hundred Hertz by dedicated wavefront sensors.

The following diagram shows the hierarchy and the dependencies between the various components of the wavefront control system. An arrow from a subsystem A to a subsystem B indicates that A imposes certain requirements on B, or more explicitly, that A can only work if certain accuracies have been reached or parameters been defined by B.

Several control loops, some of them with a critical dynamic behaviour, are combined in the non-adaptive control. A description of the architecture of the complete control system is given in the next section. The sections 7.3 to 7.5 will discuss the components of the non-adaptive control system listed above in more detail.
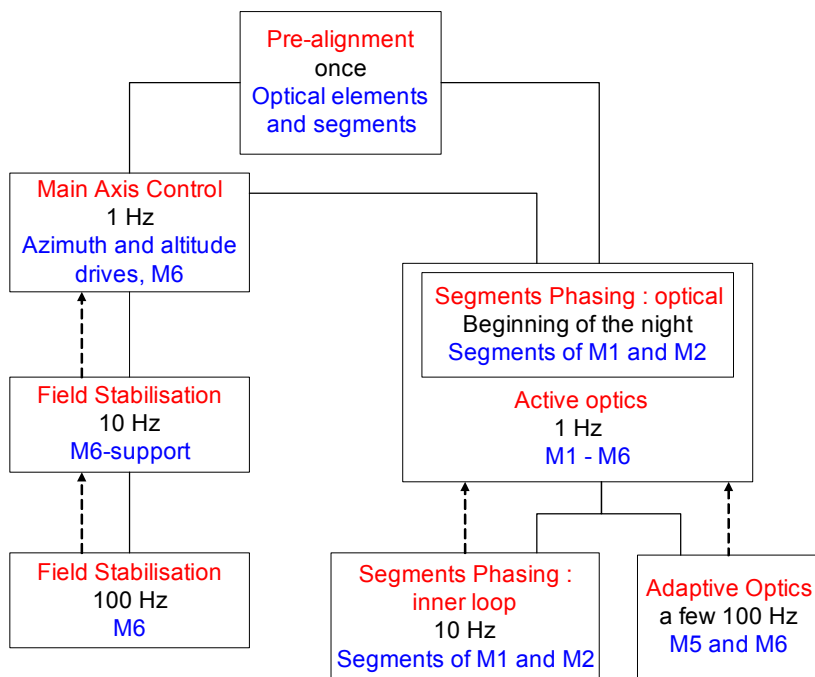

Figure 7-1. Wavefront control - overall layout.

7.2   General control architecture

OWL as an opto-mechanical system is continuously affected by two kinds of perturbations, which are the main sources of wavefront errors:

Non-adaptive wavefront control

1. Atmospheric turbulence which generates errors in the incoming wavefront.

2. Perturbations such as wind buffing, gravity deflections, thermal deformation, and friction forces, which generate wavefront errors through deformations of optical assemblies or of the structure of the telescope.

The main objective of the wavefront control system is to compensate the effects of these perturbations, and hence to correct the wavefront errors. In addition, the control system is responsible for the tracking of the telescope. Based on the nature of the perturbations such as their amplitudes and their temporal and spatial frequencies, the tasks of the telescope control system are distributed to different subsystems, with their characteristic sensors and actuators. The main control subsystems of OWL are: main axes control, phasing and segment control of M1 and M2, active optics (AcO) including M3 and M4 active deformation, field stabilization with M6 and adaptive optics (AO) with M5 and M6. The non-adaptive control subsystems shall reduce the wavefront errors to such a level that the adaptive optics control system can correct the remaining wavefront errors (including atmospheric turbulence) with the available range of its actuators.
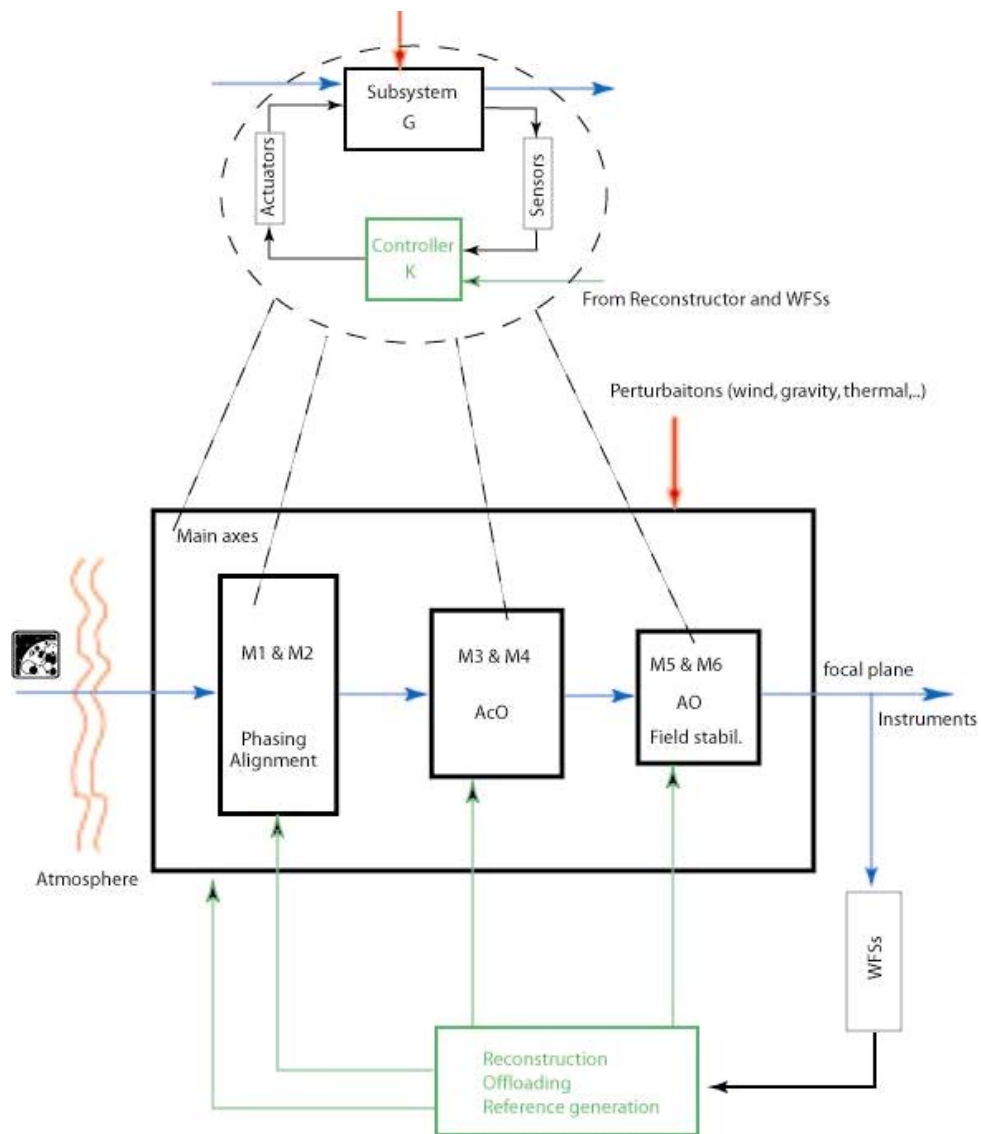
Figure 7-2 Wavefront Control Architecture for OWL

Each telescope control subsystem may be made of several hundreds control loops working simultaneously, possibly interacting with other loops in the same or in different subsystems. This

suggests that the control system is complex and thus a clear structure should be drawn to guarantee the correct and optimum functionality of the systems as a whole, i.e. a general control concept of telescope. For a large-scale and complex system [22], [23] such as OWL, an appropriate concept and architecture would be a hierarchical structure with a decentralized control.

At a lower level of the control hierarchy, each subsystem acts independently (decentralized), that is each control subsystem uses only local sensors and local actuators for closing a control loop. The main role of control at this level is perturbation rejection. Feed-forward control strategies for repeatable and predictable perturbations such as load variations or friction are foreseen. Feedback control laws should be designed for rejecting the dynamical and non-predictable perturbations such as wind buffeting. At a higher level of the hierarchy, a supervisor block receives the data from a wavefront sensor as an input. The main functionalities of this unit are the wavefront reconstruction on the one hand and the generation of optimal references for each control subsystem on the other hand. The determination of the optimal solution is based on the objectives of the control and the operational limits and constraints of the system. Figure 7-2 shows the block-diagram of the wavefront control architecture of OWL.

Since wavefront aberrations can be corrected by the control of the segments of M1 and M2, by deforming M3 and M4, by aligning the optical elements, and by the adaptive optics system, it is important to understand the combined effects of the corrections on the final measured wavefront. The constraints on the control bandwidth and limits on the stroke of the actuators of each subsystem offer guidelines for distributing the corrections to different subsystems. A general strategy is to offload or cascade the slow low order aberrations with large amplitudes from faster control subsystems to slower control subsystems, e.g. from the adaptive optics to the active optics or from the rigid body motion of M6 to the main axis or M2. However, due to the complexity of the problem it is necessary to derive the best solution from an optimization procedure.

The coupling between different control systems (optical and dynamical) should be understood and studied in detail. The separation and decoupling of some subsystems can be deduced from the time-scale separation principle. For instance, the adaptive optics control system with its relative high control bandwidth and small stroke can be decoupled from other subsystems and studied separately. However, in order to correct the effects of the wind on the telescope and to achieve the desired performance it seems that a relative high control bandwidth is required for some subsystems. This implies that there could possibly be an interaction between the actions applied by the control system and the resonance modes of the telescope structure, e.g. between the segment control system and telescope structure coupled through the segment support structure, or tip/tilt control of the M6 unit and corrector. Although these interactions are expected to be small because of the large mass ratios between the subsystems, they should be analyzed in detail and taken into account in the design of the controllers.

The local control loops should be designed based on the dynamical models as well as on the available knowledge about the disturbances acting on the system. Robust controllers should be chosen to guarantee the stability and the performance in the presence of modelling errors and uncertainties. In addition, to be able to increase the control bandwidth without the risk of exciting the resonance modes, active vibration damping and isolation techniques must be applied where needed [20].

In this section, the dynamical performance of the tracking with the main axes and the field stabilization by tip/tilt movements of M6 are investigated. There are two main sources of perturbation on the structure, wind buffeting on the one hand and torques due to rolling friction acting on the wheel/track interface of each friction drive unit on the other hand. The objective of the control system is to minimize the tracking errors with the main axes and the residual wavefront errors with the M6 tip/tilt unit in the presence of perturbations. Control strategies for improving the performance of the system are proposed. The performance of the closed-loop system is verified by simulations.

7.2.1   Wind rejection

The most important disturbance acting on the telescope structure is wind buffeting at different locations in the structure. Due to the large mass and the low resonance frequency of 2.6 Hz of the locked rotor mode only a limited control bandwidth is available. In addition the dynamical behaviour of the telescope and the influence of the wind loads on the main axes vary significantly with the altitude angle of the telescope because of variations of the resonance frequencies of the structural modes with the altitude position of the telescope. In many applications PID (Proportional-Integral-Derivative) controllers achieve a satisfactory performance. They can often be used for processes that are difficult to control provided that no extreme performance is required. However, if the performance has to be pushed to the limits, as it is the case with the stringent specification (1 arcsec RMS) for the tracking error with the main axes, other well-adapted types of controllers should be chosen. Good candidates for such a task are polynomial controllers [11], [15] which have been used in the simulations in this section.

The design of robust controllers for the azimuth and altitude axes is based on the dynamical models of the telescope structure. The details of the design and the results of the simulations for 4 altitude angles (zenith, 30 deg, 45 deg, and 60 deg) and two wind directions (frontal, lateral) are documented in RD17.

The main idea behind the design is to parameterise a controller that reshapes the control sensitivity function, i.e. the closed-loop transfer function from wind load perturbation to the main axis position, in such a way that the error is minimized for the frequencies where the effect of wind is most important. The block diagram of a multivariable closed-loop system describing the underlying control problem is presented in Figure 7-3, where G represents the transfer function between the input forces from the bogies[59] and the measured output $y(t)$ ('main bearing angular position' for altitude and 'central bearing angular position' for azimuth axis). K is the controller transfer function and H represents the transfer function from wind load forces to the output measurements.
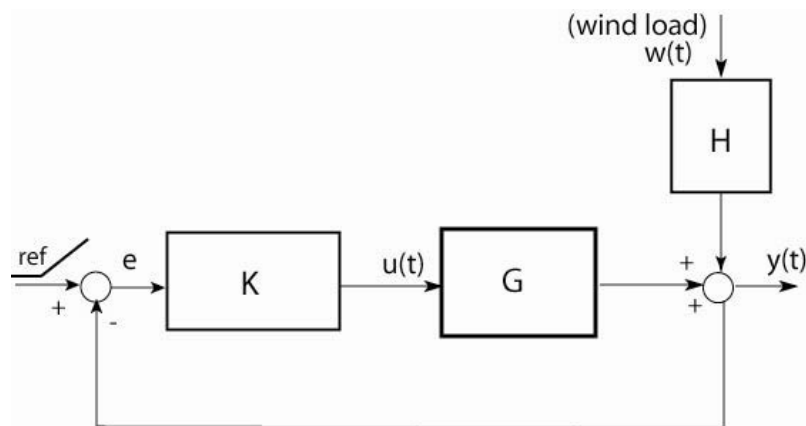

Figure 7-3 Block diagram of the closed-loop system

---

[59]   In this part of the study, bogies are considered as rigid, and the force introduced by a bogie is the sum of the forces (torques) generated by the motors attached to the wheels of the bogie.
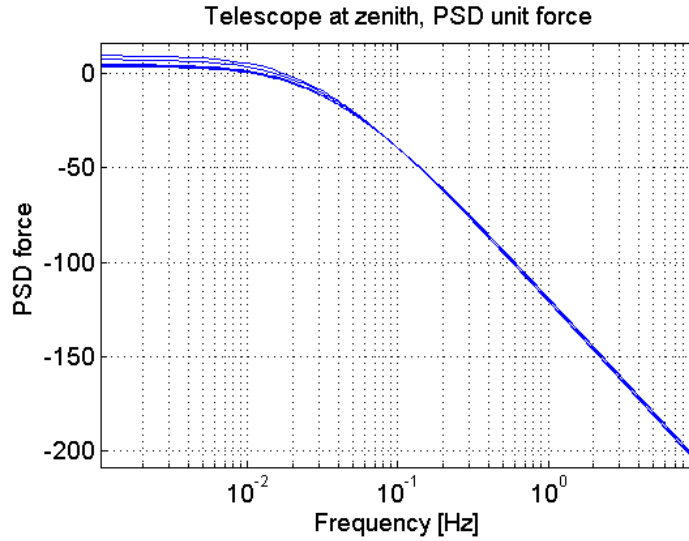
Figure 7-4 Normalized PSD of the wind loads applied to different height: altitude configuration

To proceed, models of the wind loads and a model of the telescope structure are required. Wind buffeting is a stochastic phenomenon and thus the Power Spectral Density (PSD), either of the speed or of the aerodynamics load, is a convenient way to characterize it. The PSDs which are used for this study are given 5.4.1.1.1.2). They are calculated for different heights from ground, i.e. for different wind speeds starting from 10m/s in lower heights and increasing up to 14 m/s at the top of the telescope. Time signals (wind force) with equivalent statistical characteristics can be obtained from these spectra. These perturbations are applied at five different sections of telescope structure (see RD527). Figure 7-4 shows the normalized power spectral densities of the wind forces for the altitude axis with the telescope pointing to the zenith. Here 'normalized' means that PSD is divided by the static wind force acting on specified telescope areas. However, during the simulations the PSD will be multiplied by the actual average force which scales with the wind speed.
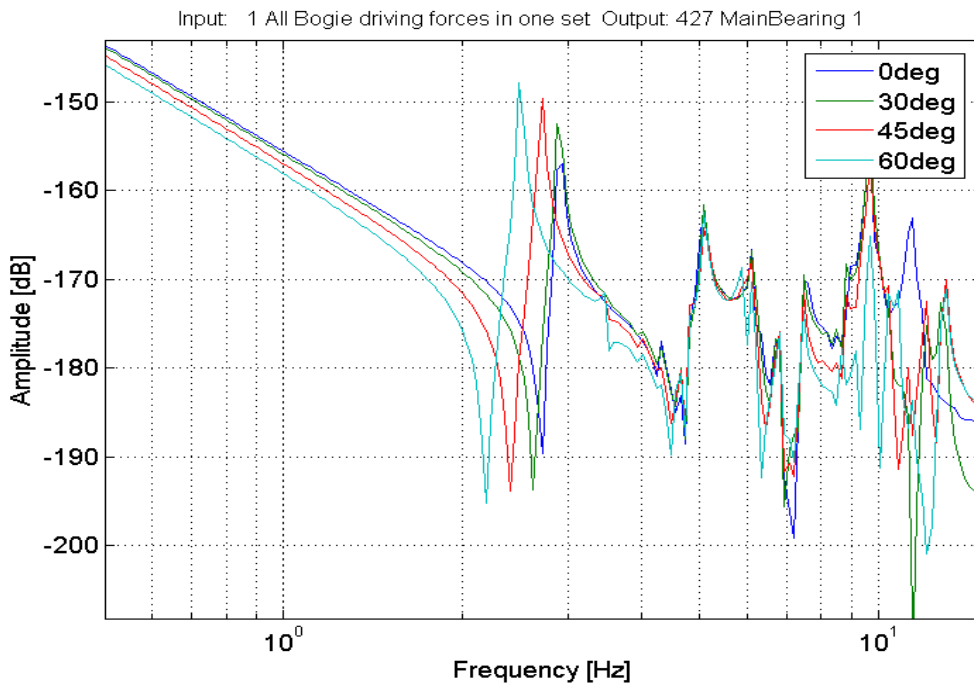

Figure 7-5 Frequency characteristics of altitude models for four different configurations

Non-adaptive wavefront control

Based on finite element analyses, state-space models for different configurations have been created. These configurations can be divided in two groups for the control of the azimuth or the altitude axis. There are four altitude configurations corresponding to four different zenith distances: 0 deg (zenith), 30 deg, 45 deg and 60 deg, and two azimuth configurations corresponding to two zenith distances of 30 deg and 60 deg. To be able to use these models for the control design, the order of these models has been reduced. The models are available as continuous state-space objects in Matlab. For more details about configurations, corresponding models, and model reduction the reader is referred to RD527.

The frequency characteristics of the models (*G*) for four altitude configurations and two azimuth configurations are shown in Figure 7-5 and Figure 7-6, respectively.

Figure 7-5 shows that the natural frequencies of the first resonant mode of the altitude models decrease from the zenith to the 60-degree configuration with those of the zenith and the 30-deg configurations being very similar. Figure 7-6 shows that the dynamics of the azimuth models for the 30 degree and the 60 degree configurations are also nearly identical.

Robust controllers are now designed with the objective of tracking errors of less than 0.3 arcsec RMS, taking into account the system and disturbance models. The nominal models used for the design of the controllers for both axes are the reduced order models of the telescope at 30 degrees. Their robustness is verified for the other configurations. The details of the design procedure are given in RD17. The desired closed-loop bandwidths for the altitude and azimuth axes are chosen as 1.8 Hz and 0.6 Hz, respectively. The corresponding control sensitivity functions for both axes are shown in Figure 7-7 and Figure 7-8 respectively. The effect of the rejection of the effects of the wind load can be observed in Figure 7-9 which compares the PSDs of the open- loop responses with the PSDs of the closed-loop responses. The controller reduces the PSD errors significantly for frequencies up to 1Hz.
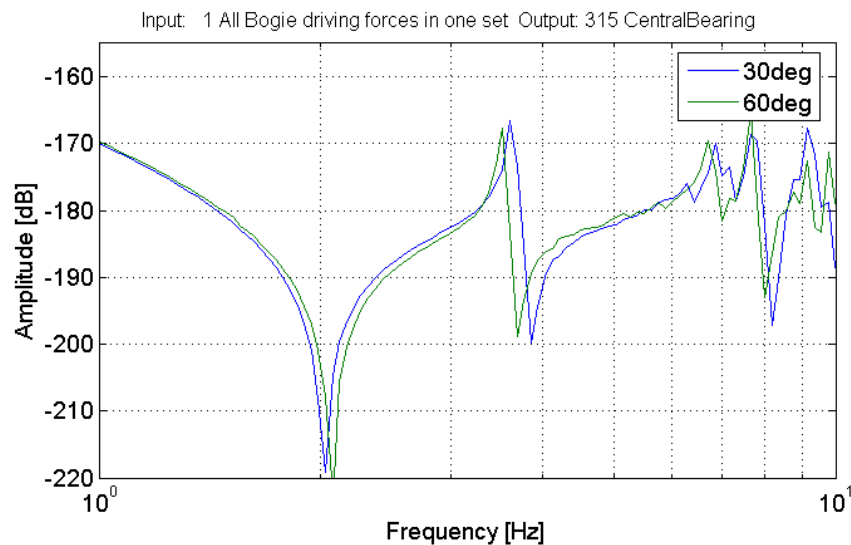

Figure 7-6 Frequency characteristics of azimuth models for two different configurations
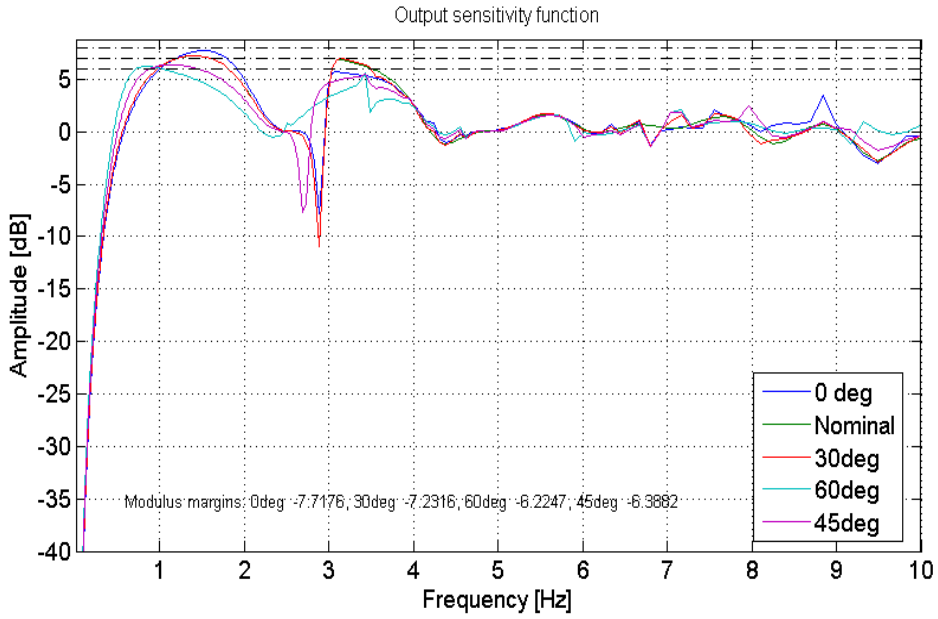
Figure 7-7 Output sensitivity function as a a measure of both the rejection of perturbation and the robustness for the altitude axis

A simulation has been done for the closed-loop system (both axes and different configurations) with a ramp reference signal having a slope of 0.5 arcsec/sec. The tracking error (main bearing of the altitude axis) for the 30-deg configuration is shown in Figure 7-10. The controller is tested for all available telescope configurations. The results are summarized in Table 7-1 and Table 7-2. They show that the requirement of a modulus margin of less than -8dB is always fulfilled with the chosen design.
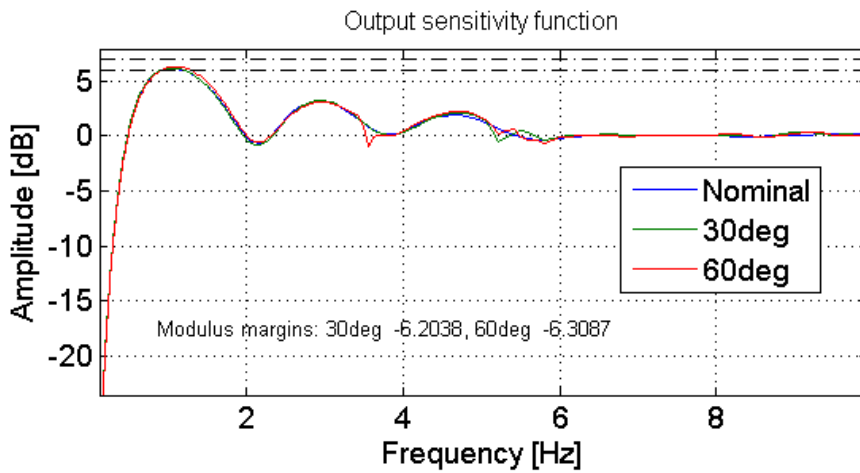

Figure 7-8 Output sensitivity function as a measure of both the rejection of perturbations and the robustness for the azimuth axis
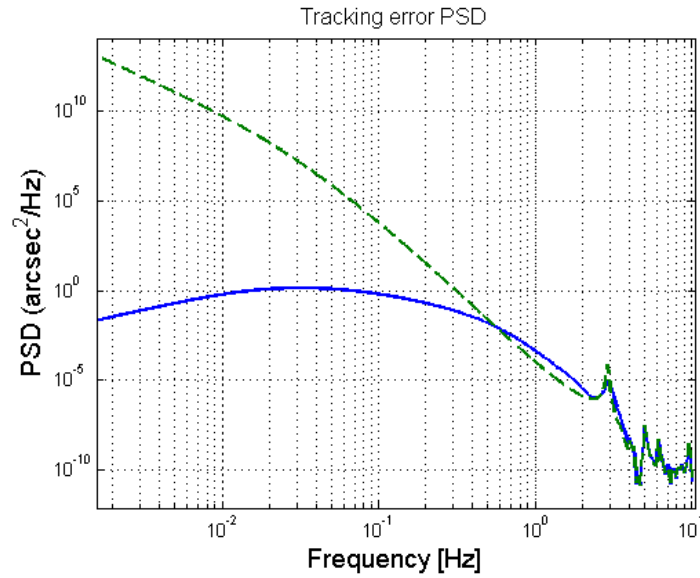
Non-adaptive wavefront control

Figure 7-9 PSD of tracking error on the main bearing (altitude axis 30 deg) – open-loop (dashed), closed-loop (solid)
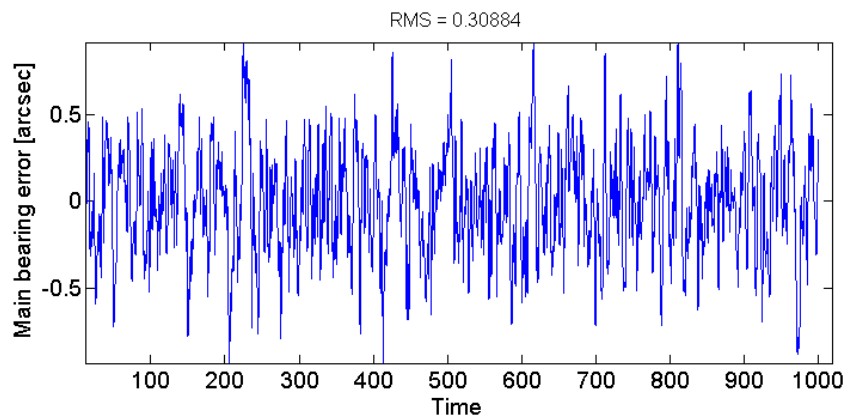

Figure 7-10 Main bearing (altitude axis) tracking error for 30 deg configuration

zenith distances	Modulus margin [dB]	Main Bearing RMS error [arcsec]
0 deg	-7.7	0.19
30 deg	-7.2	0.31
45 deg	-6.3	0.27
60 deg	-6.2	0.32

Table 7-1 Altitude axis: summary of the design results

zenith distances	Modulus margin [dB]	Central Bearing RMS error [arcsec]
30 deg	-6.2	0.044
60 deg	-6.3	0.036

Table 7-2 Azimuth axis: summary of the design results

7.2.2   Friction compensation

Friction drives, also called bogies, are used for the main axes of the telescope. The description of the friction drives and the bearing system is given in section 9.4.5.1.3. The azimuth axis will be equipped with about 250 units distributed on eight tracks and the altitude axis with about 150 units on two elevation cradles. They ensure a homogeneous load distribution on the structure. Each bogie consists of four spherical or cylindrical wheels which are independently driven by brushless ring torque motors. One of the main sources of tracking and positioning errors on the main axes of the telescope is the 'rolling' friction torque acting on the wheel/track interface of each bogie. Close to zero velocity the friction force is a nonlinear function of the velocity and the applied force (see Figure 7-11). In the control of systems with friction the undesirable effects are oscillatory motions around the desired reference trajectory due to stick-slip events. In recent years, extensive research on modelling, identification and compensation of friction have been done. For a comprehensive survey of the approaches and some promising results the reader is referred to [17].
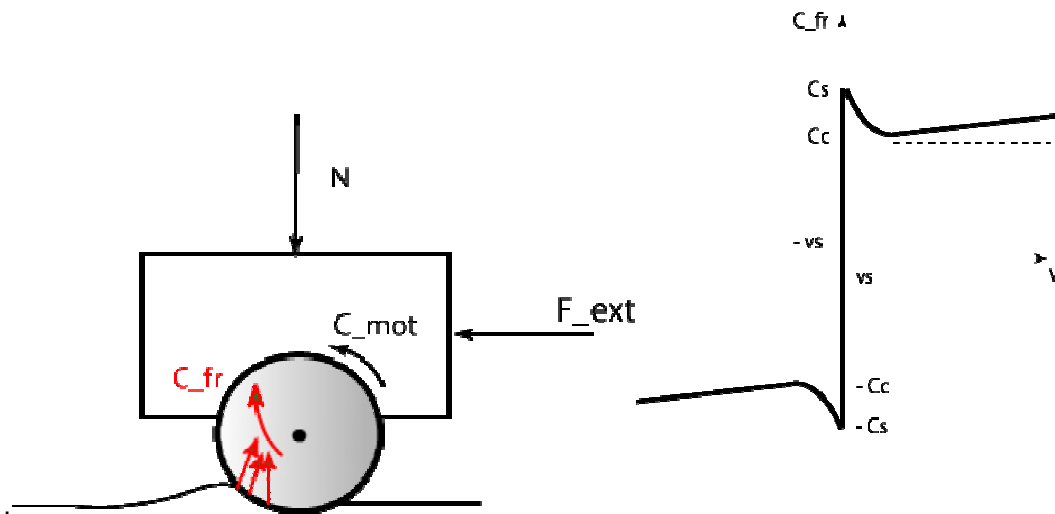

Figure 7-11 Left) bogie subjected to various forces-- Right) friction as a function of velocity

The effect of the non-linearity of the friction on the wheel/track interfaces of the bogies and the control strategies for the compensation of the friction have been studied in RD14, RD15, and RD18. Here, the approach and the main results are summarized.

- In order to distinguish the friction related effects from other oscillatory behaviours related to the telescope structure, first a dynamical model of a bogie was created with the telescope represented by an 'equivalent inertial mass'. Two different friction models, LuGre [19] and Karnopp [18], were used for the friction on the wheel/track interfaces. Both models capture the stick-slip effect. The LuGre model in addition captures the properties related to micro displacements of two surfaces in the pre-sliding regime. Stick-slip effects occur only if the telescope is moving at very low velocities. Figure 7-12 shows the stick-slip oscillation when the telescope is tracking in closed loop with a reference velocity of 0.1 arcsec/sec (main axes). For a higher reference velocity like 0.5 arcsec/sec the stick-slip effects disappear.
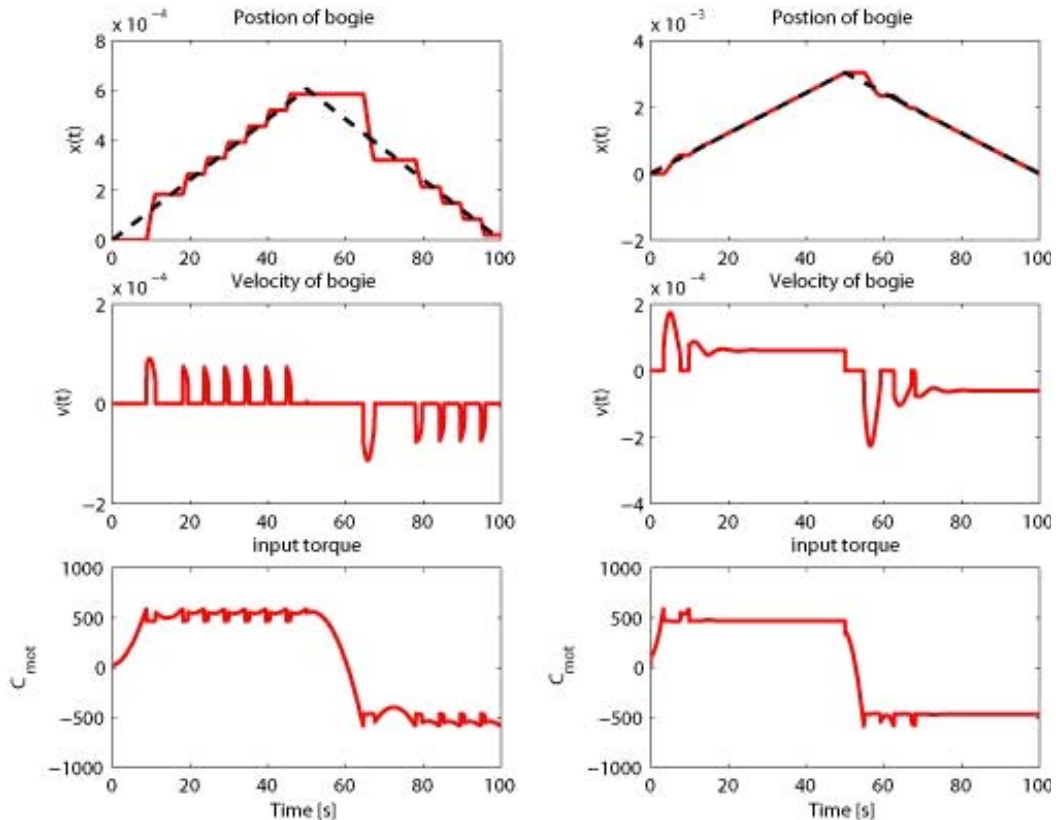
Non-adaptive wavefront control

Figure 7-12. Tracking a ramp reference signal in closed-loop. Left: slope 0.1 arcsec/sec stick-slip motion. Right: slope 0.5 arcsec/sec; stick-slip disappears.

There are two main approaches for friction compensation:

- A non-model based approach using mainly stiff, i.e. high gains proportional and derivative terms in the feedback controller. The advantage is that the approach is robust since the feedback controller is used for the rejection of the perturbations. However, since only a limited closed-loop bandwidth for the control of the main axes of telescope is available, the use of high gain parameters in the controller is neither feasible nor advisable.

- A model based compensation method which consists of two steps, first an estimate of the friction, i.e. an identification of friction model parameters, and second, an application of a feed-forward control term based on the estimate of the friction in the first step to cancel the effect of the friction.

- A model-based friction compensation strategy is proposed for an interconnected system of bogies (see RD15). The block diagram of the control strategy is shown in Figure 7-13.

  Some of the bogies may be 'passive', i.e. they will not be equipped with motors. Since passive bogies do not have any control input the effect of friction on those bogies has to be compensated by the 'active' bogies by adapting the feed-forward compensation term. If the interconnections of the bogies are not perfectly rigid as it is in reality the nonlinear effects of the friction on the passive bogies cannot instantaneously be eliminated by a control action (see RD15) Therefore, oscillations can be introduced in the system due to a stick-slip motion on the passive bogies[60], as can be seen in Figure 7-14 showing the results of a closed-loop simulation of seven interconnected bogies where one is considered to be passive. This problem could be solved either by increasing the stiffness of connections, increasing the damping through a selection of appropriate lubricants for the wheel/track contact surface, or ultimately making all bogies in azimuth axis active. This issue will be

---

[60] Stick-slip with relative small amplitudes compared to the case friction is not compensated.

Non-adaptive wavefront control

investigated in detail in the framework of the ELT Design Study: 'Characterization of Friction Drives and Bearings' (see RD514).
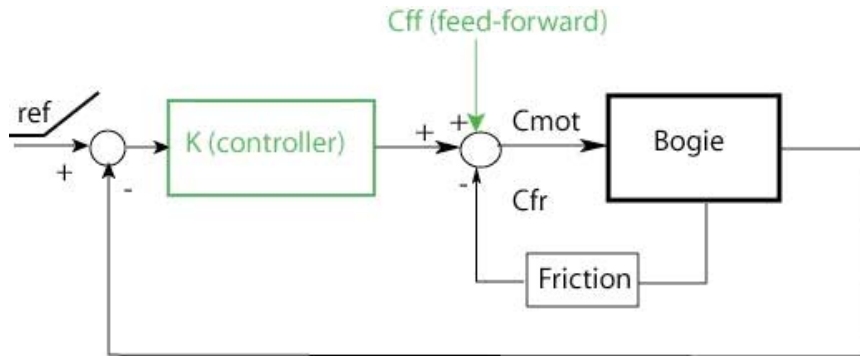
Figure 7-13 Block-diagram of bogie control system: feedback + feed-forward friction compensation strategy
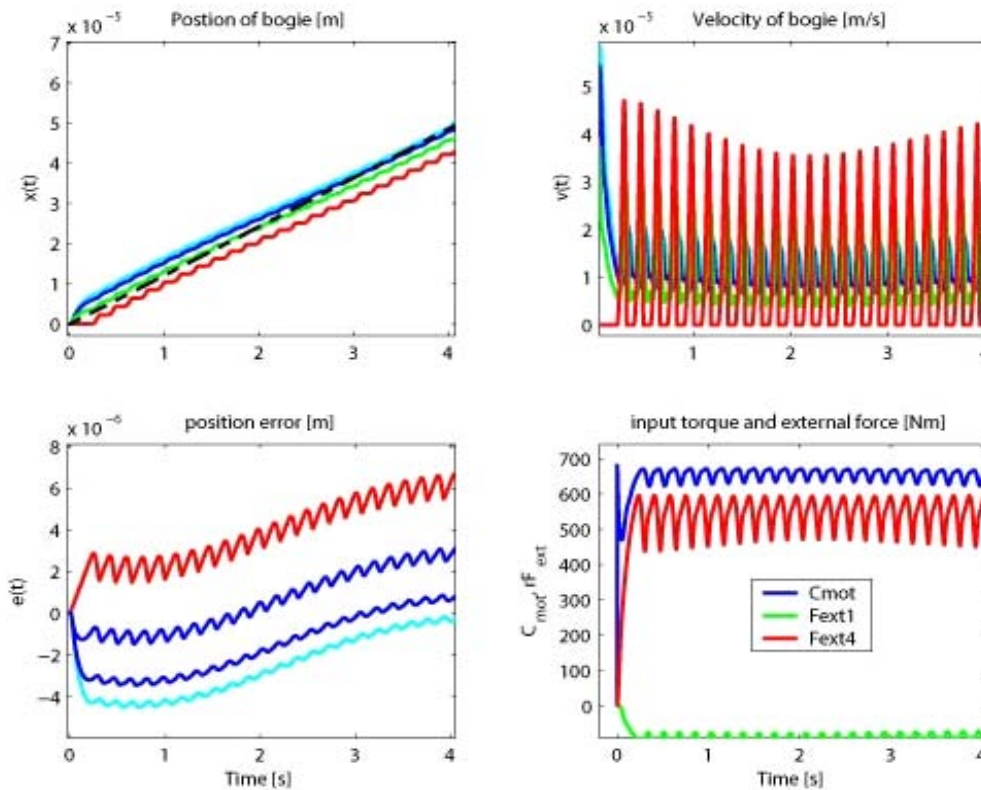

Figure 7-14 Closed loop simulation of seven bogies (with friction compensation), one bogie is passive which exhibits small stick-slip motion, oscillations are induced on other bogies.

- Since the compensation strategy relies on pre-defined friction models, the influence of variations of the model parameters has been investigated. Even if the two key parameters in the friction model are over- or underestimated by as much as 20% the effect of stick-slip events can still be compensated (see RD15). The guidelines for estimating the friction parameters are discussed in RD18.

- As stated earlier, in the initial approach the telescope has been modelled by a rigid body with an equivalent inertia. Such an assumption provided a good insight into the problem and gave some guidelines for the control strategy. To verify the efficiency of the approach a complete dynamical state-space model of the telescope has been generated by finite element (FE) analyses and a procedure applied to reduce the model. Bogies are

Non-adaptive wavefront control

represented as pure force generators. The friction models, which include the non-linear effects, have been incorporated into the state-space models for the azimuth and altitude axes at bogie points (see RD16). Figure 7-15 shows the results of a simulation for the closed-loop response of the altitude axis in the absence and the presence of the feed-forward friction compensation. Note that here the feed-forward compensation is considered to be ideal, i.e. based on a perfect knowledge of the friction parameters. The effect of a mismatch of friction parameters is discussed in RD15.
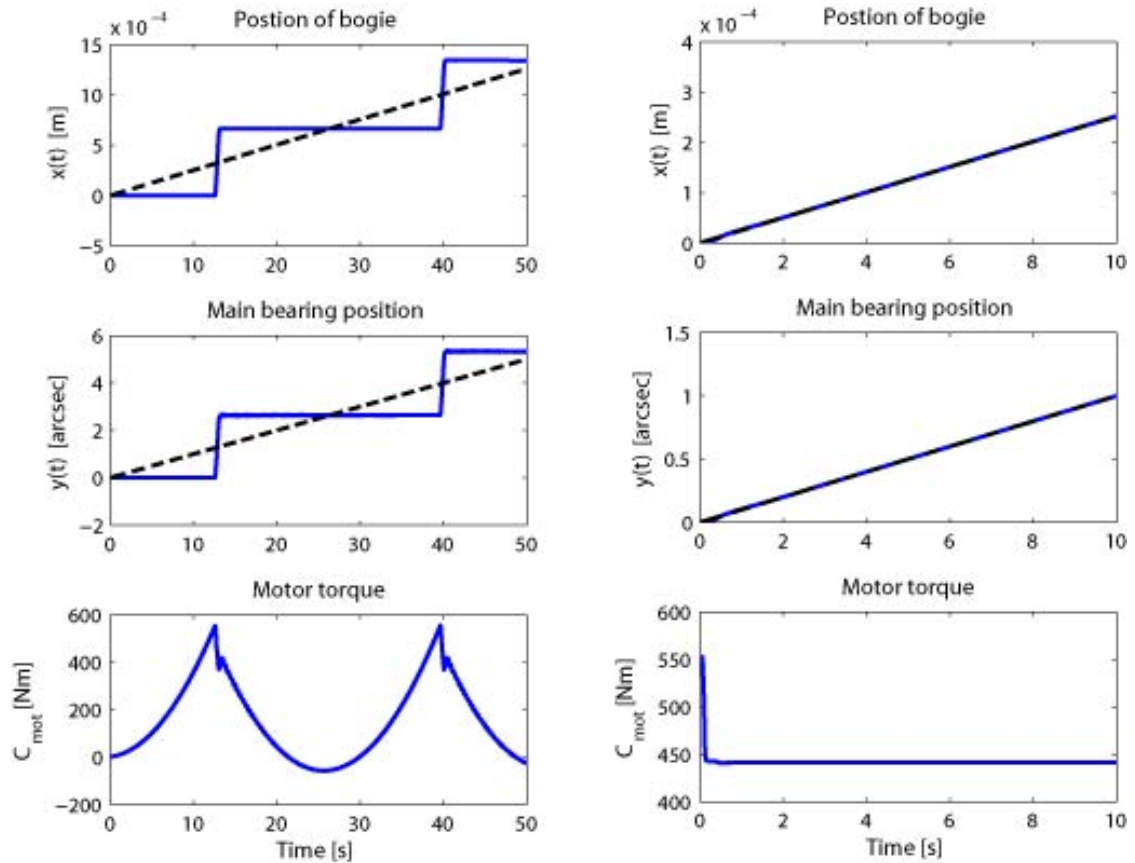
Figure 7-15 Closed-loop simulation of the altitude axis at 30 deg tracking a ramp reference signal with a slope of 0.1 arcsec/sec: left) no feed-forward friction compensation---right) with feed-forward friction compensation

- Finally, in the last stage the closed-loop behaviour of the system has been simulated in the presence of both wind load and friction perturbation. The overall control strategy is to read the main axis encoder position errors and apply the polynomial controller designed for the wind rejection. The controller generates the input torque to the system at each bogie point. The local feed-forward friction compensation is applied to each bogie (see RD17, RD16). Figure 7-16 shows the simulation results for the altitude axis in the 30-deg configuration tracking a ramp reference with a slope of 0.1 [arcsec/sec].
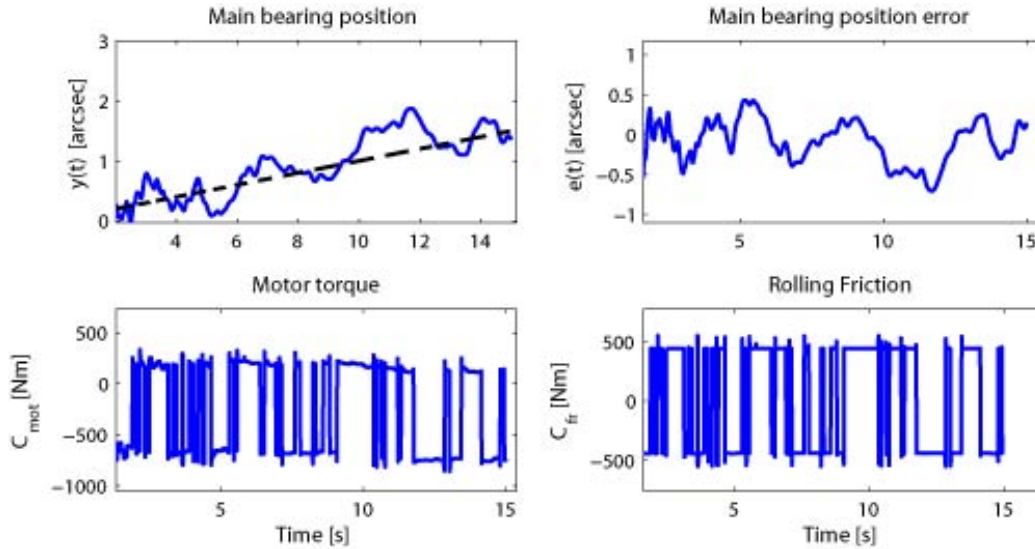
Figure 7-16 Closed-loop simulation of altitude, 30-deg configuration

7.2.3   Field stabilization

One of the main tasks of M6 is field stabilization, i.e. fast tip/tilt correction of residual tracking errors induced by wind buffetting on the structure. This would be achieved in two steps, with a coarse stage for large amplitudes and fine correction with the adaptive shell. In the following we show that a bandwidth of a few Hz for the coarse stage would be sufficient to reduce errors to within the expected range of the thin shell.

As shown in the previous section, the effect of the wind on the main axes can substantially be reduced by an appropriate control of the main axes. An efficient perturbation rejection on the main axes also reduces, due to the coupling of the main axes to the rest of the structure, the effect of wind on the whole structure including support structures of mirrors. However, the residuals are still too large for the correction capabilities of the adaptive thin shell of M6. To reduce the errors to values within the correction range of the thin shell, the bulk of the residual tip/tilt errors should first be corrected by the M6 tip/tilt control unit.
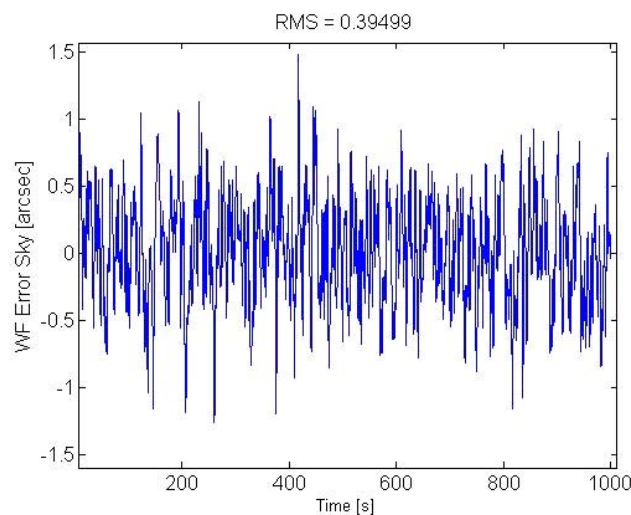

Figure 7-17 Wavefront error (tilt) on the sky- Altitude simulation: zenith configuration, main axis control with different wind loads applied to different levels

Apart from deformations of the individual optical elements, wavefront errors due to wind buffeting are produced by rigid-body movements, that is misalignments, of the optical elements.

Non-adaptive wavefront control

To get an estimate of the amplitudes and frequencies of the misalignments of all mirrors in six degrees of freedom the closed-loop response of the complete OWL structure to a wind from the –y direction has been simulated. The effects of the obtained misalignments on the wavefront are computed with the optical sensitivity matrix of OWL (see RD2). Figure 7-17 and Figure 7-18 show the tilt components of the wavefront error in sky coordinates as time series and PSDs for the zenith configuration.
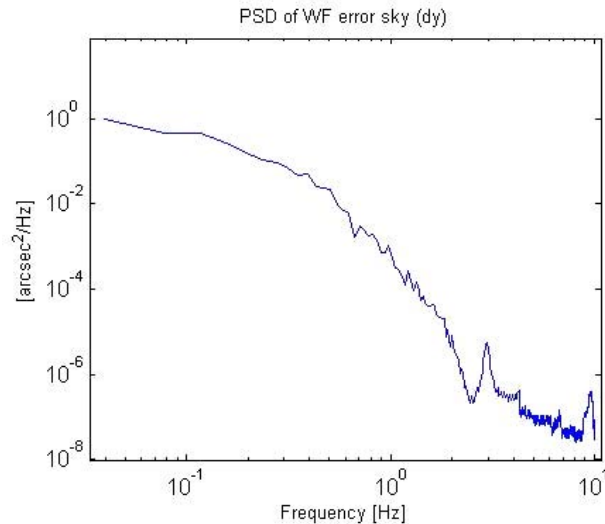
Figure 7-18 PSD of the wavefront error (tilt) on the sky

Field stabilization can be achieved by steering the M6 unit actively. The wavefront error has been calculated as a function of the control bandwidth[61]. The result is shown in Figure 7-19 and indicates that with an ideal control an accuracy of 0.01 arcsec can be achieved with a closed-loop bandwidth of about 1Hz (and prior to adaptive correction).
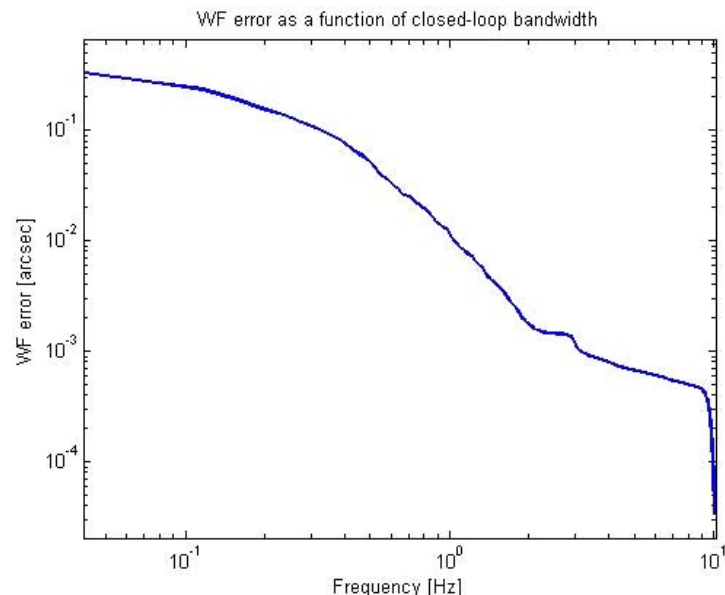
Figure 7-19 Wavefront error (tilt) after field stabilization correction as a function of the closed-loop bandwidth

---

[61] It is assumed that the closed-loop control rejects the perturbation 'perfectly' up to the closed-loop bandwidth and is not effective elsewhere. Although such perfect control action is not realistic, it gives a first estimate about the lower limit of the required closed-loop bandwidth.

Non-adaptive wavefront control

A 2-degree-of-freedom model of M6 has been constructed. The dimensions of the M6 unit are given in Section 9.4.5.5. The mass of the mirror is estimated to be about 500 kg (Zerodur mirror), and the frequency of the first resonance modes for the tip and tilt motions are assumed to be 60 Hz. The ensueing wavefront error, that is the image tilt, can again be obtained with the help of the optical sensitivity matrix. The closed-loop control scheme is shown in Figure 7-20. The objective is to design a controller *K* which minimizes the residual wavefront error, seen as a perturbation in the control loop. *G_M6* represents the transfer function between torque generated by actuators and the tip and tilt motions of the M6 unit.
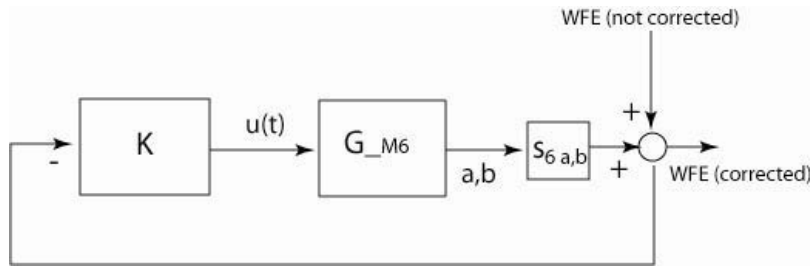
Figure 7-20 Block diagram of the closed-loop control of M6: field stabilization

The design of the controller K depends on the PSD of the uncorrected wavefront error and the dynamical model of the M6 unit. The bandwidth of the control system is provisionally defined as 2 Hz. Figure 7-22 shows the time series obtained in a simulation of the closed-loop response of the M6 unit. The closed-loop control of the tilt motion of M6 improves the performance to the an accuracy of approx. 0.01 arcsec RMS. Figure 7-21 compares the PSD of the tilt wavefront error before and after the field stabilization.
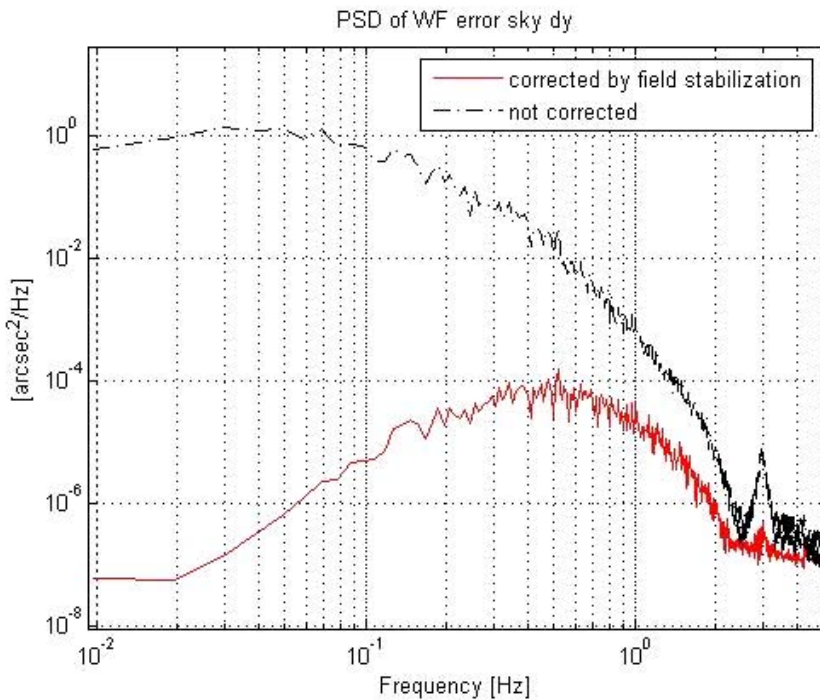
Figure 7-21 PSD of the corrected tilt wave front error on the sky

Non-adaptive wavefront control

Figure 7-22 Simulation results: wavefront errors before and after correction, tilt motions of the M6 unit and the input torque applied to the unit.

The residual M6 tilt corresponds to actuator strokes of 0.25 mm. The reaction forces to the movements of the actuators could excite the support system of the M6 unit and the structure of the corrector. To avoid undesirable resonances, the M6 unit may be be isolated from the support system by a compensation mass moving in the direction opposite to the mirror as in the M2 unit of the VLT [28]. Currently the conceptual designs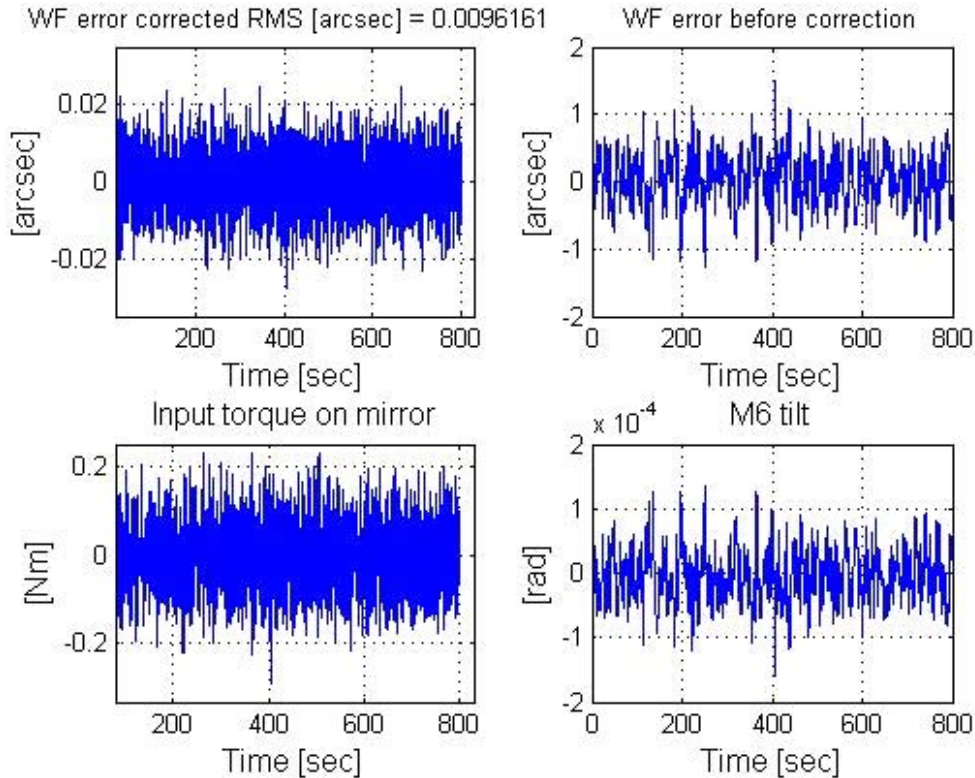 of the M6 unit, taking into account the issue of resonances, are going on under ESO contracts.One possible solution for reducing the required stroke on the actuators is to offload the correction in the very low frequency range to the main axes or eventually to M2. Figure 7-19 shows that the wavefront error can be reduced by a factor of three, if tilt corrections are done by the M2 unit at frequencies up to 0.2 Hz. As a consequence, the stroke needed for corrections with M6 would be reduced. As M2 is segmented, the feasibility of such an overall tip/tilt motion of M2 will be addressed and studied in Phase B.

7.3   Pre-alignment

In a perfectly aligned telescope the optical axes of all mirrors are congruent with the mechanical axis of the adapter. Initially, at the end of the installation, the mirrors will be misaligned with respect to the axis of the adapter, the flexible meniscus mirrors will be deformed, and the segments of the segmented mirrors will be misaligned in piston as well as in tip and tilt. At this stage automatic means used by the active optics for the correction of the errors may fail because the errors may exceed the limits the optical analysis methods can cope with. The following pre-alignment procedure will reduce the wavefront errors to levels acceptable for the active optics system.

Non-adaptive wavefront control

1. The segmented mirrors can be coarsely aligned with the help of the edge sensors. These must be glued to the rims of the mirrors with an accuracy of approximately 200 micrometers with respect to the front surface of the segment. By moving individual segments and detecting when adjacent sensors go out of range, the differential displacements between the mirrors at the locations of each pair of sensors can be measured. From the data of all pairs of sensors the optimum movements of all segments, which minimize the rms of the differential displacements, can be calculated and applied. At the end of this procedure the rms of the errors due to segment misalignments, excluding the effects of the undetectable segment defocus mode, should be of the order of a few hundred micrometers.

2. With the help of a spherometer, positioned at the corners of the newly installed segments, the piston errors can be reduced to a few nanometers. The correction of the defocus mode will be left to the stage of the automatic corrections.

3. All other mirrors could be aligned with respect to its neighbours starting from M6 based on the input from the fibre extensiometer. This requires an installation of fibre links between specified locations on all pairs of successive mirrors.

Finally, a second round of aligning the segments in tip and tilt in the segmented mirror could be done on-sky by stacking the images from the individual segments. Because of the small ratio of the size of the subapertures corresponding to the segments on M1 to the overall size of M1 such a stacking will also correct the comparatively low spatial order effects of any misalignments of the mirrors or of any elastic deformations of the meniscus mirrors on the wavefront. This is of course only true for the field position of the wavefront sensor unit used for stacking the images. The image quality should, for this field position, only be limited by the wavefront errors of individual segments, by the accuracy of the stacking itself, and by piston phasing errors of the segmented mirrors. However, at other field positions, additional wavefront errors due to still existing mirror misalignments and elastic deformations still exist.

At the end of the pre-alignment, we expect residual errors to be within the following range:

- Misalignments of the mirrors as rigid bodies:
    - Positions of M1 and M2: approximately 1 mm
    - Positions of M3, M4, M5 and M6: approximately 0.5 mm
    - Tilts of M1 and M2: approximately 2-3 arcseconds
    - Tilts of M3, M4, M5 and M6: approximately 1 arcsecond

- Deformations of the meniscus mirrors:
    - M3 and M4: approximately 30 micrometer wavefront r.m.s.
    - M5 passive: at most 2 to 3 micrometer wavefront r.m.s.
    - M6 and the adaptive M5: depends on the design, but is assumed to be small if the positions on the front surfaces of the adaptive mirrors are measured against a reference surface.

- M1 defocus mode : no empirical data available.

From this point on the remaining errors can be deduced from simultaneous measurements with wavefront sensors distributed over the field and be corrected by rigid-body realignments of the mirrors, corrections of the shapes of the meniscus mirrors, and alignments of the individual segments within the segmented mirrors.

7.4　Active optics

7.4.1　Introduction

The purpose of the active optics system is the correction of all types of wavefront aberrations introduced by comparatively slow misalignments and surface deformations of the optical elements in the telescope at low temporal frequencies. The expected focal surface in the adapter is the reference surface, where all measurements of the errors which are introduced by the misalignments and the deformations are made. From these measurements one has to identify the sources of the wavefront aberrations. This is not straightforward since the wavefront errors generated by different mirrors may completely or at least to a large extent compensate each other in the focal surface. The error sources can in some cases only be distinguished from each other by analysing comparatively small field dependent effects. On the whole, the problem is quite complex with two segmented and four flexible mirrors, even if a few of them generate only a restricted set of wavefront errors.

A very formal way of solving this problem would be to write down a vector of all significant error sources and another vector of a sufficient number of possible aberrations at various locations in the field. Assuming that a linear description is sufficient, the connection between the two vectors is established by a so-called influence or sensitivity matrix. A singular value decomposition of this matrix would show which set of well distinguishable measurements would be generated by which set of well distinguishable error sources. The corresponding eigenvalues would show the significance of each pair of measurements and sources. Such an approach would also show groups of sources which could be well separated from each other. In addition those error sources can be found whose effects are effectively indistinguishable in the focal surface. Because of the large number of segments and mirrors this procedure leads to a very large matrix which may be difficult to invert. In addition, it may not give much insight into the effects of the various error sources. Therefore, the following procedure splits the correction into three steps, described in the three following sections: the alignment of the segmented mirrors, the correction of surface deformations of the individual mirrors, and the alignment of the mirrors regarded as rigid bodies.

7.4.2　Alignment of the segments in M1 and M2

Since only a small number of segments will be added to M1 and M2 at a time one can assume that most of the segments of these mirrors are already well aligned. The alignment of the segments, especially the newly installed ones, will be done with the following procedure at the beginning of the night.

1. Based on measurements with one of the Shack-Hartmann sensors all segments can be aligned in tip and tilt. With sufficiently bright guide stars the wavefront errors will be of the order of at most a few nanometers over each subaperture corresponding to one segment. Because of the large number of segments, especially in the primary mirror, the slopes of the smooth low-order aberrations in the wavefront, generated by misalignments or deformations of the other mirrors, are effectively constant over the small subapertures corresponding to individual segments. These slope errors can therefore to a large extent be corrected by appropriate tilts of the segments. For a given low-order aberration the residual aberrations over a given segment subaperture are well defined. This effect is referred to as scalloping. Under the assumption that the deformations of the individual segments are small the slopes of the wavefront are well corrected, at least for the field position of the Shack-Hartmann sensor. The residual major wavefront error is then generated by piston steps at the interfaces of adjacent segments.

2. The piston steps at the interfaces of adjacent segments are measured by optical sensors using multiple wavelengths techniques. The goal of this correction is to reduce the piston steps to less than 100 nm and therefore to avoid the 2π ambiguity in subsequent narrow-band measurements.

3. Narrow-band measurements with bright stars, which can reach accuracies of a few nanometers for the estimate of the piston steps, will be used to align the segmented mirrors. At this point there are two possible ways of proceeding with the alignment.

  o Correction of piston errors only.

    The basis for such a correction will be the average of the piston error along each intersegment edge. The segmented mirrors would then be well aligned in piston, but not in tip and tilt, since the individual segments are still compensating the slope errors introduced by the other mirrors. These low spatial frequency wavefront errors have to be corrected at a later stage by measuring scalloping effects or field aberrations. Because of the propagation of the noise σ_n in the measurements of the piston steps the rms σ_1 of the wavefront error introduced by this correction will be $\sigma_1 \approx 0.5\sigma_n$ [37], [38]. With σ_n expected to be of the order of a few nanometers, the wavefront error due to segment piston errors will therefore be negligible.

  o Correction of piston, tip and tilt errors.

    The basis for such a correction will be two measurements of piston steps along each intersegment edge, giving both the relative average piston error and the relative tilts at the edges of adjacent segments. After this correction the segmented mirrors will be aligned in piston, tip and tilt, but the effects of the slope errors generated by the other mirrors and the rigid-body misalignments would reappear in the final wavefront. To prevent this, the differences in the wavefront slopes before and after the alignment of the segments in the segmented mirrors have to be offloaded to the other mirrors as changes in rigid-body alignments or changes of the shapes of M3 and M4. If the optical sensor is not capable of detecting relative tilts perpendicular to the edge, but only relative piston displacements, an appreciable amount of the segmented mirror defocus mode may exist. Because of the propagation of the noise σ_n in the measurements of the piston steps the rms σ_2 of the wavefront error introduced by this correction will, excluding the error due to the defocus mode, be approximately $\sigma_2 \approx 15\sigma_n$ [37], [38].

    The readings of the edge sensors, which in the current design are also not capable of detecting the defocus mode, will be stored as reference values for the continuous closed-loop alignment corrections of the segmented mirrors via the edge sensors.

The second option of the ones described above will be the baseline.

4. The correction of the M1 and M2 defocus modes can be left either to the stage where all the mirror deformations will be corrected or it can be done by measuring so-called scalloping effects, as described below. The M1 and M2 defocus modes with constant slopes over individual segments has already largely been compensated during step 1 of this procedure by a smooth defocus aberration generated by the changes of the shape of the monolithic mirrors M3 and M4 or by axial displacements of mirrors. The residual aberration is a defocus aberration that is identical on all the individual segments. A Shack-Hartmann sensor with 19 lenslets in each subaperture corresponding to one segment can measure this differential defocus, and therefore the coefficient of the M1 and M2 defocus modes. Because of the large number of photons available with long integration times of the order of 100 seconds even the differential defocus on a single segment can be measured with an accuracy of a few nanometers. Owing to the large number of segments the error in the overall differential defocus will then be negligible. After the correction of the defocus modes the segments of the primary and secondary mirror will be aligned.

7.4.3   Correction of mirror deformations

Deviations of the shapes of the large meniscus mirrors M3 and M4 from their ideal shapes can be due to optical manufacturing and to incorrect support forces. From the experience with the VLT the initial wavefront aberrations of M3 are expected to be of the order of 20 μm rms for 3rd order astigmatism and 3 μm rms for trefoil. For M5 the corresponding figures are expected to be

of the order of 3 μm and 0.5 μm. Because of the elastic properties of the meniscus mirrors the deformations in the form of elastic modes decrease rapidly with the order of the modes. The highest modes which are, for large changes of the telescope altitude angle, appreciably affected by the support forces with systematic variations of their coefficients of the order of 20 nm are modes like the lowest mode of rotational symmetry six and the third mode of symmetry zero. The lowest 30 elastic modes are therefore sufficient for the description of the errors in the mirror shapes of M3 and M4.

As in the VLT, a sampling of the wavefront with 20 by 20 subapertures over the pupl is sufficient for an accurate estimate of the coefficients of all these modes. The size of the subapertures on M1 is then approximately 5 meters by 5 meters. In the VLT stars of magnitude 13 deliver, with integration times of 30 seconds, a sufficient number of photons to reduce the errors on the coefficients of the wavefront aberrations due to photon noise to less than the errors introduced by the atmosphere [41]. Since the area of a subaperture in OWL is approximately 100 times larger than the area of a corresponding subaperture in the VLT one can either choose shorter integration times of the order of one second or use fainter stars. In principle, this would offer the possibility to apply closed-loop corrections of mirror deformations and alignments at frequencies up to approximately 1 Hz. However, for such short integration times, the effects of the atmosphere, in particular the effects of the limited size of the isoplanatic angles have to be investigated.

The major problem in a telescope with several deformable mirros is to distinguish in the final wavefront the contributions generated by the individual mirrors, since errors introduced by one mirror can be compensated by errors introduced by other mirrors. The wavefront analysers cannot distinguish between aberrations generated by the deformations of mirrors which are conjugated to each other. Therefore, the effects of the deformations of M1, M4 and M6 are indistinguishable. Also M2 falls into this group since it is sufficiently close to the pupil. However, if the mirrors are not conjugated to each other, such compensations are in general only effective for one field angle, leaving additional wavefront aberrations at other field angles. If the deformations are expressed in terms of Zernike polynomials, these field aberrations can be calculated analytically if the center and the radius of the imprints of the beam on the mirror are known for arbitrary field positions [39] [41].

This is shown in Figure 7-23. The footprints of the beam on M3 are different for different field angles. The Shack-Hartmann sensors therefore sample different areas of M3.

Therefore, in principle, one should be able to distinguish between the aberrations generated by M3, M4 and the group M1, M2, M4 and M6.

The measurement of the aberrations over subapertures of the mirrors is similar to the measurement of aberrations introduced by layers in the atmosphere conjugated to these subapertures. Techniques developed for adaptive optics can therefore be applied to the active optics wavefront sensing [42], [43]. First tests in this direction have shown promising results.

The dependence of these additional aberrations on the field position is different from the field dependence of the additional field aberrations generated by rigid body misalignments. They can therefore be distinguished from each other if a sufficient number of sensors is available in the field.

In OWL the ratios of the shifts of the centers of the beam to the radii of M3 and M5 for a field radius of 1 arcminute are approximately 0.01 for M3 and 0.04 for M5.

The field aberration generated by 3rd order astigmatism is only a special type of distortion. For a field angle of 5 arcminutes a deformation of 20 μm on M3 is equivalent to an apparent shift of the sky position of 0.01 arcseconds. The deformations of the different mirrors in form of 3rd order astigmatism can therefore effectively not be distinguished from each other by measurements in the focal surface.

A deformation in form of trefoil generates 3rd order astigmatism with a linear radial dependence and a more complicated angular dependence. For 3 μm of trefoil on M3 the modulus of the additional 3rd order astigmatism is approximately 150 nm at the edge of the field and therefore detectable. However, within the inner field with a radius of 1 arcminute the modulus is only of the order of 30 nm.
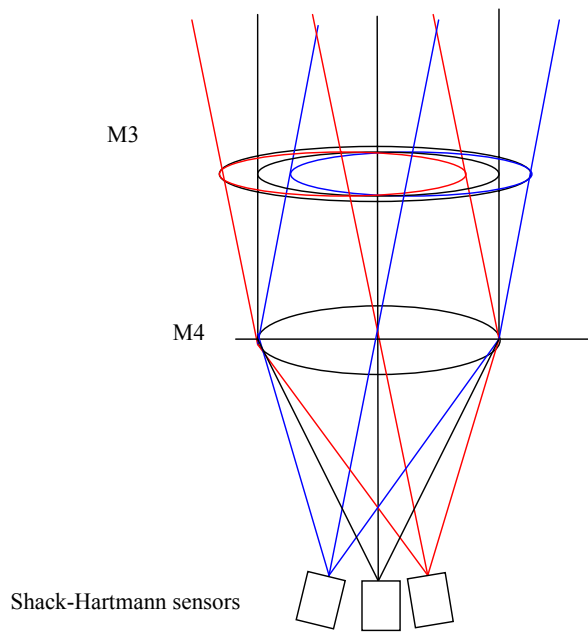
Figure 7-23. Field of View of the Shack-Hartmann sensors on M3 and M4.

The effects of deformations in form of higher order modes is even smaller and it may therefore be sufficient to distinguish only the trefoil deformations coming from M3, M5 and from the group M1, M2, M4 and M6. However, it is no problem to extend this type of analysis to a larger set of modes [40]. Since the radial field dependencies of the aberrations generated by higher modes may not be linear, wavefront sensors are required at at least three different moduli of the field angles. With a total of six sensors at at least three different orientations of the field angles a sufficiently large number of field aberrations can be measured. This has been confirmed by simulations in [40].

7.4.4   Correction of the rigid-body alignment of the mirrors

In general, rigid-body misalignments of the individual mirrors in five degrees of freedom will generate aberrations in addition to the nominal aberration of the centered optical system. These additional aberrations are characterized by their field dependencies. Lateral displacements of the flat mirrors M2 and M6 do not generate aberrations. In total, there are 26 degrees of freedom for the generation of wavefront aberrations with rigid-body movements of the individual mirrors. The number of wavefront sensors required to measure the 26 unknown parameters can be estimated as follows.

1. The expansion of the Hamilton characteristic function up to fifth order contains 26 types of aberrations, where the non-rotationally symmetric aberrations like third order astigmatism with a quadratic field dependence have been counted twice. This set contains 15 different Zernike polynomials. The larger number of terms in the expansion means that the same Zernike polynomial can occur with different field dependencies.

2. Field distortions and field curvatures may be difficult to measure due to a limited accuracy of the positioning of the guide probes. If one neglects these types of aberrations the number of terms in the Hamilton characteristic function is reduced to 18 and the number of Zernike polynomials to 13. The maximum field order in the expansion terms is quadratic.

3. At a given field location only the coefficients of the Zernike polynomials can be measured. To obtain the full information one has to measure also the field dependence of these coefficients. This requires, for a quadratic field dependence, at least three sensors at different radial field positions. For the non-rotationally symmetric coefficients one also needs to know their orientation which requires at least three sensors in azimuth direction.

Therefore, six sensors, all measuring the coefficients of 13 Zernike polynomials, should be sufficient to determine the 18 unknown parameters.

Simulations for a three-mirror telescope are presented in [39]. Six wavefront sensors measuring a total of 78 coefficients will also be sufficient to include the estimate of shape deformations discussed in the previous section.

An additional complication is that field-independent aberrations generated by alignment errors can be corrected by deformations of the pupil mirrors M4 and M6. If this was the case these aberrations would reappear after a correction of the alignment and the corresponding surface deformations of M4 and M6 would have to be removed.

Ideally, all alignment corrections would avoid changes of the pointing of the telescope. For the powered mirrors only rotations around their centers of curvature would then be permitted restricting the correction capabilities. However, such a restriction would only be required if the pointing model was made without the active optics system in operation. Therefore, a final pointing model has to be done for all sky positions with a fully aligned telescope under the control of active optics.

7.4.5   Relationship between various types of aberrations

Three different types of wavefront aberrations due to telescope errors will be present in OWL.

- Pure optical aberrations, which are described by Zernike polynomials. These aberrations are predominantly generated by rigid-body misalignments of the mirrors.

- Elastic deformations of monolithic mirrors which are described by the elastic modes of the monolithic mirrors.

- Modes introduced by the propagation of errors in the measurements of piston steps at intersegment boundaries. In the low order limit these modes can be described by Bessel functions [38].

The active optics system has to take the conversions between these mathematical descriptions into account, for example, when sets of coefficients of field aberrations determined by the optical design and described by Zernike polynomials, have to be subtracted from related sets of coefficients of elastic modes measured at the field positions of the wavefront sensors.

7.4.6   Operation with adaptive optics

Whenever the adaptive optics corrections are applied by M5 or M6, most of the slowly varying errors introduced by the telescope optics will first be corrected by the adaptive optics system. After a while, because of the accumulation of the often large lowest order aberrations, the actuators of M6 will run out of their correction range. M5 and M6 will then have to download some of their corrections of the wavefront errors due to the telescope optics to the other mirrors controlled by the active optics system.

These adaptive optics corrections by M5 and M6 provide, however, only a partial correction of the wavefront errors introduced by the telescope. M6 and M5 will only correct aberrations which are conjugated to the ground layer, which is close to the pupil, and to a layer at approximately 10 km, which is conjugated to M5. Aberrations generated by surface deformations of M3, which is neither conjugated to M5 nor to M6, or by rigid-body misalignments can only partially be corrected by M5 and M6 for arbitrary field positions..

The active optics wavefront sensors could then still measure these accumulating field aberrations. Even between downloads from the adaptive optics system the active optics system could then correct alignment and shape errors of individual mirrors based on the information about the aberrations at several field positions. Upon a download from the adaptive optics system, the active optics system would then only redistribute those aberrations that could not be attributed to a specific mirror, to one or more mirrors depending on the available ranges and range margins of those mirrors.

7.5 Phasing

7.5.1 Phasing strategy

One of the specific tasks associated with segmented telescopes is *phasing*, requiring an active control of the position of each individual segment in three degrees of freedom: translation along the optical axis (piston) and rotation about two axes perpendicular to the optical axis (tip-tilt). Three hardware systems are required for the *active segment control*: *capacitive or inductive edge sensors* which provide real time information about the relative segment displacements, *segment actuators* which compensate for these displacements, and a *phasing camera*. The inner loop with the edge sensors and the actuators is a fast correction for the segment displacements with a bandwidth of approximately 10 Hz, running continuously during the operation of the telescope. The phasing camera traces the slow changes in the wave front shape, providing the new reference values for the edge sensors.

The calibration of the edge sensors is performed once at the beginning of the night. An alternative concept would be to operate the phasing camera also during the operation of the telescope with a frequency of approximately 0.03 Hz and then recalibrate the edges sensors with the measurement of the phasing camera. This option is valid provided that a sufficiently bright reference star for the phasing camera can be found in the field of view.

The unphased telescope would have the resolution of the aperture of one segment and will deliver images full of speckles. To decrease the speckle effects to a level which would not exceed the residual errors after adaptive optics corrections, the remaining tolerable wavefront error, due to the misalignment of the segment, has to be less than 30 nm RMS. The importance of the phasing of segment mirrors in a telescope has been demonstrated in several papers [83], [84], [85].

The analysis in this section is restricted to the correction of the piston, tip and tilt errors of the segments. During the operation of the telescope the phasing corrections are based on signals from edge sensors at intersegment borders. An optical phasing procedure that is done at the beginning of the night with bright stars will supply the reference values for the edge sensors.

Two of the OWL mirrors will be segmented. Section 7.5.4.6.4 presents a technique to disentangle the segmentation errors of M1 and M2.

7.5.2 Blind phasing

Blind phasing is meant for segment alignment without on-sky metrology. Normally, blind phasing would be performed only during integration of the system, prior to first light, or during daytime re-integration of segments after off-line maintenance.

The concept is still very notional. Segments would be re-integrated into the aperture by means of a movable handling tool located inside one of the mirror covers (see also 13.2.1.4). Once the load transfer from the tool to the segment support is completed and interfaces are locked, the handling tool, fitted with position sensors, would be used as a spherometer. Adjacent segments, already in place and phased to the accuracy of the position sensors, would serve as calibrating gauge for the spherometer.

Spherometry measurements are made by optical manufacturers to sub-micron accuracy. The accuracy requirement for OWL handling tool-spherometer will eventually have to be in line with the capture range of on-sky phasing calibrations, which is expected to be at least a few microns (multiple wavelength). Should a higher accuracy be required, the contact measurements could be replaced by interferometric ones, using a dual wave interferometer (same principle as for APE internal metrology, see appendix A-1.2).

7.5.3 Position sensors

In existing segmented mirror telescopes the edge sensors use capacitance measurements. This is a proven technology which reaches accuracies of the order of a few nanometers RMS. However, capacitance measurements are sensitive to environmental conditions as for example high relative humidity. A different technology, which can reach the same accuracies, but is less sensitive to environmental factors, is based on inductance measurements.

The flat electrodes used for the capacitance sensors are replaced by a set of coils. Edge sensors using this technology will be developed within the ELT study in the FP6 programme (see appendix A-1.2 belowA-1.2. The most important specifications are a noise of less than 0.2 nm RMS / sqrt(Hz) within the frequency bandpass from1 Hz to 100 Hz and of less than 5 nm RMS / sqrt(Hz) within the frequency bandpass from 6e-6 Hz to 1 Hz, a measuring range of +/- 5 mm, and an absolute accuracy of 0.1% of the measuring range.

7.5.4 On-sky calibrations

7.5.4.1 Optical Phasing

This section presents various techniques which have been developed and proposed for the optical phasing of the segments, and also results of simulations and laboratory tests if available. One of the techniques for optical phasing is analysed in more detail.

Without optical phasing the misalignments of the segments can be of the order of several micrometers (see also 7.5.2), which is a problem for the narrow-band phasing sensors suffering from a 2π ambiguity. This can be solved with multi-wavelength techniques.

Three new phasing camera concepts are currently studied: the curvature sensor, the pyramid sensor, and the spatial phase filtering sensor. The basic principle for all three techniques is a modification of the wave front reflected by the mirror surface in such a way that the amplitude of the detected wave conveys the information about the phase discontinuities or the derivatives of the wavefront. This amplitude coding is achieved by a defocusing of the beam in the curvature sensor, by a spatial filtering in the image plane in the pyramid, and spatial phase filtering in the last sensor.

7.5.4.2 On-sky phasing techniques - overview

Different concept of phasing camera have been developed worldwide, some of them are based on wavefront sensors used in adaptive optics. All phasing cameras presented below have the capability to measure piston and tip-tilt misalignments. A brief description of these sensors is given together with some results of simulations and laboratory tests. Most of these sensors will be compared with each other within the APE project which is part of the FP6 program.

7.5.4.2.1 Modified Shack-Hartmann technique

This application of the Shack-Hartmann technique has first been proposed first by Chanan [86] and been used for the phasing of the segments in the Keck telescopes. Lenslets or optical devices with a similar functionality focus the light from circular subapertures centered on points on the interface between two neighbouring segments as shown in Figure 7-24 on the left hand side. A slightly modified version could be used for OWL, where the two circular lenslets on each edge are replaced by one cylindrical lenslet covering the full length of one edge, as shown in Figure 7-24 on the right hand side. The information about the phase steps is primarily obtained from changes in the diffraction pattern, as shown in Figure 7-25 for monochromatic light and no disturbance by the atmosphere.. The PSF has one maximum when the two segments are phased and two decentered peaks when for a piston of $\lambda/2$.
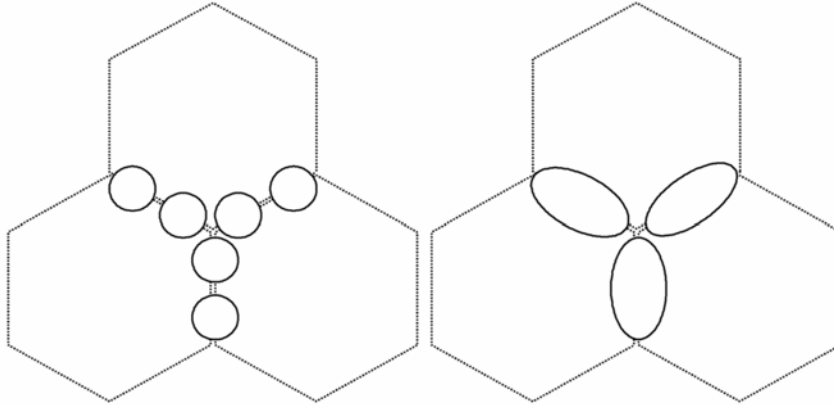
Figure 7-24. Two types of lenslet and their projection onto the edge of the segments
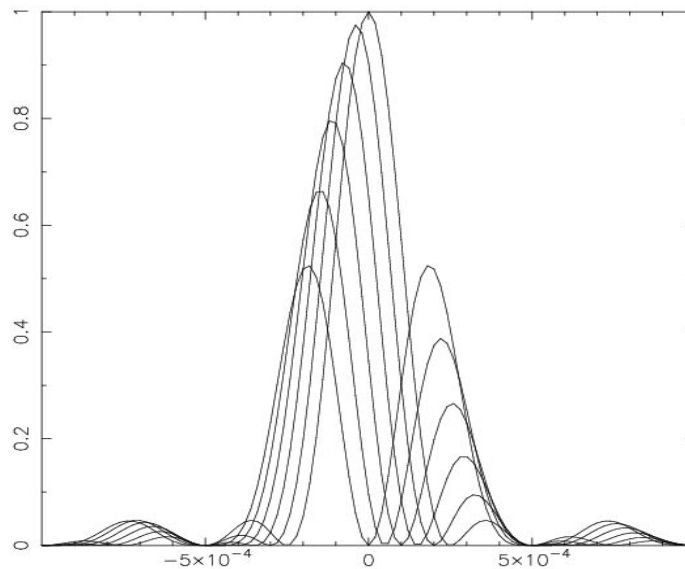

Figure 7-25. Shape of the PSF for piston steps ranging from 0 to λ/2.

7.5.4.2.2   Modified Mach-Zehnder technique

The concept of the Modified Mach Zehnder, shown in Figure 7-26, has been developed at the Laboratoire d'Astrophysique de Marseille (LAM) [87][88].

The general principle of this modified Mach-Zehnder interferometer is to introduce a spatial filter at an intermediate focus in one of the two arms and to use the light from that arm as a reference. After recombining the light of the two arms the signal is concentrated near the borders between the segments with an amplitude which depends on the piston step, the phase difference between the two arms and atmospheric disturbances as shown in Figure 7-27.

The difficulty with this sensor is to set and maintain a specified optical path difference between the two arms, and to align the two arms to avoid shearing effects and defocussing. K. Dohlen from LAM has proposed a concept, called phase filtering technique, which avoids such alignment problems.
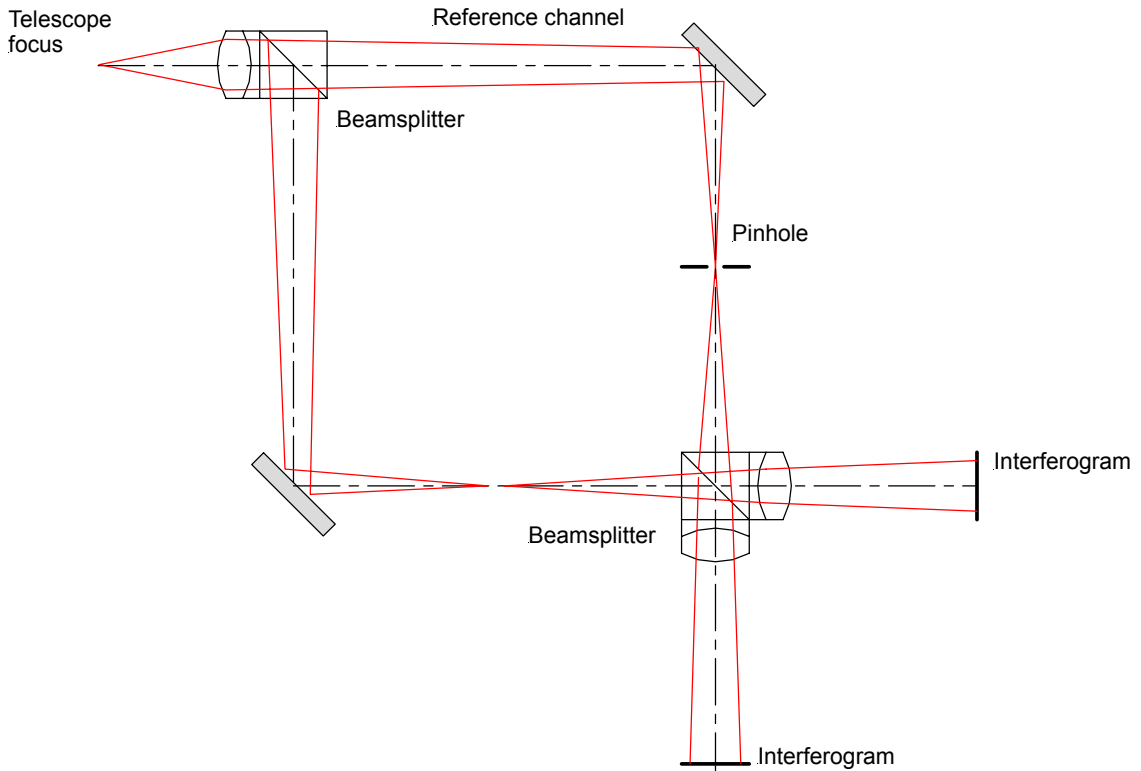
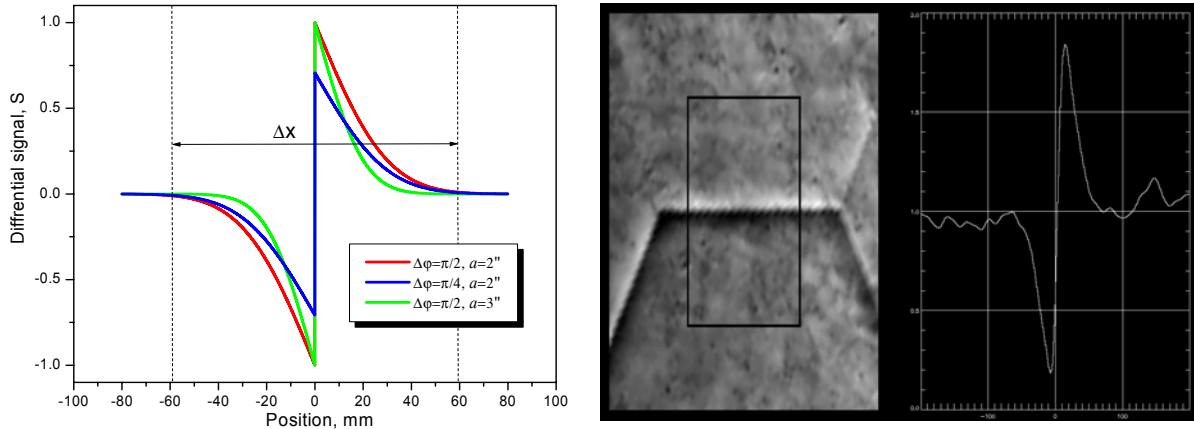Figure 7-26. Conceptual setup of a Modified Mach-Zehnder interferometer.

Figure 7-27. Mach-Zehnder signal profile for a piston step of π/2 and for different optical path differences between the two arms. Theoretical predictions are on the left hand side and experimental results on the right hand side.

7.5.4.2.3   Phase filtering technique

The image of the star is filtered by a phase plate which is made of a transmissive mask with a diameter of the size of the full width at half maximum of the seeing disk (around 0.6 arcsec) etched onto a glass plate as shown in Figure 7-28. The purpose is to introduce an optical path difference between the center and the outer regions of the image.

This mask is placed at the focus of the telescope and the segmented mirror is imaged onto a CCD by a lens. A typical OPD for the phase mask is around λ/9, which is 75 nm at a wavelength of 675 nm. Figure 7-29 shows the signal obtained with a mechanical piston step between two segments of 230 nm and an OPD introduced by the mask of λ/9.
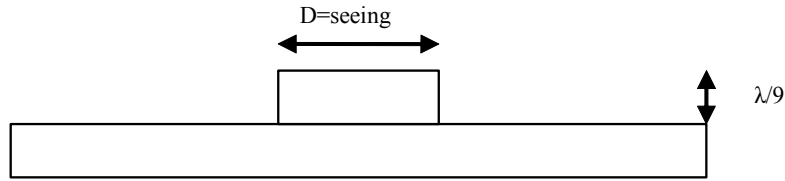
Figure 7-28. Phase mask principle.
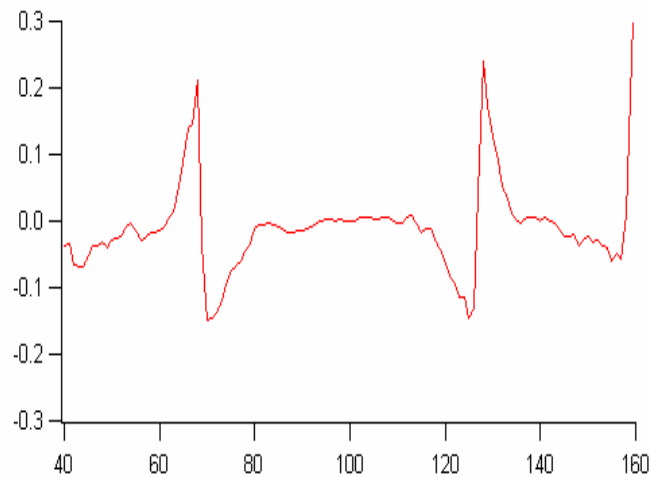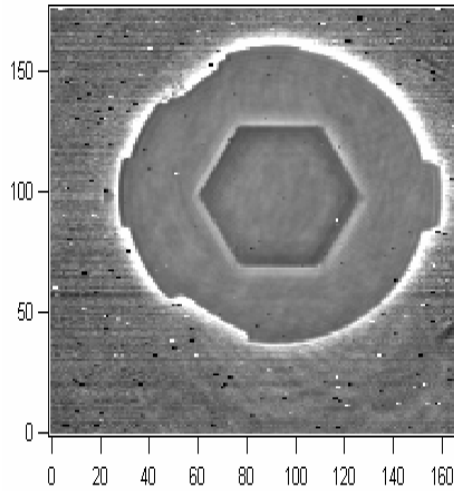
Figure 7-29. Signal obtained with a mechanical piston step of 230 nm.

7.5.4.2.4   Diffraction image technique

The concept has been developed by A. Schumacher R. Gonzales and J. Fuensalida at the Instituto Astrofisica Canarias (IAC) [94], [95] and at Keck [96]. The technique is based on curvature sensing [93], a method well developed and frequently applied in adaptive optics systems. The principle of the diffraction image technique is to take a defocused image of the segmented mirror. An example is shown in Figure 7-30.
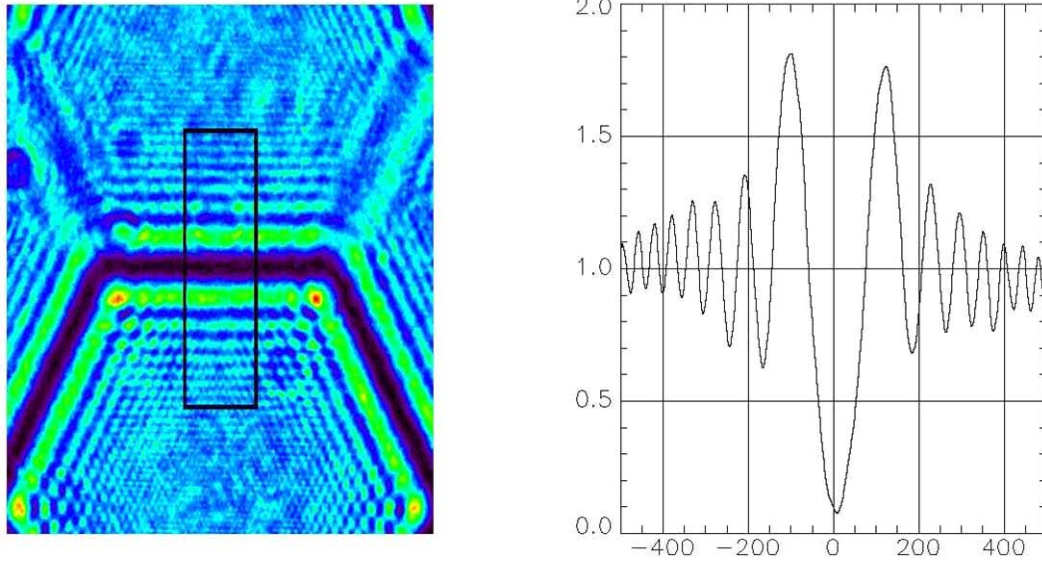
Figure 7-30. Signal obtained with the diffraction image technique (courtesy A. Schumacher)

7.5.4.2.5 Pyramid technique

This technique, first developed at the Osservatorio Astrofisico di Arcetri for wavefront sensing in adaptive optics, has also been proposed for the measurement of piston steps in segmented mirrors [97]. It is a two-dimensional knife edge test, linearised by appropriate movements of a glass pyramid. Figure 7-31 shows the signal created by a piston step between square segments.
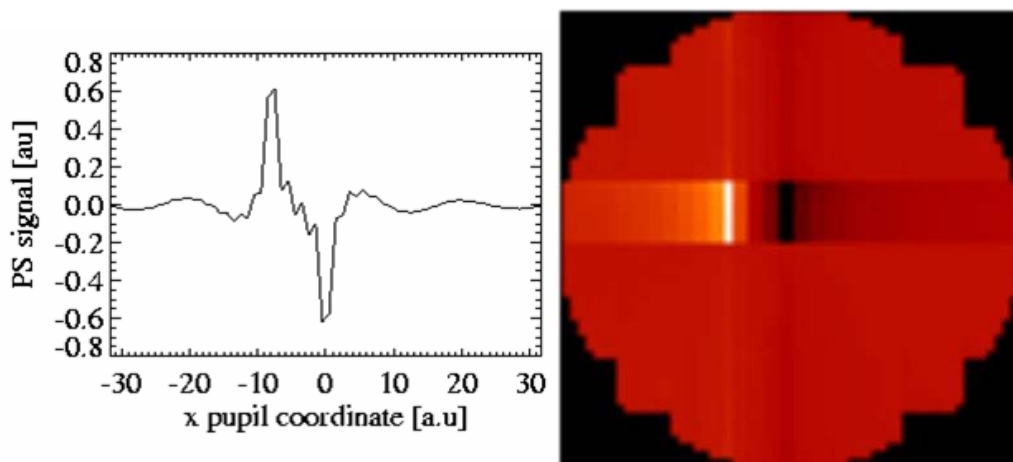
Figure 7-31. Signal obtained with the pyramid sensor for a piston step between square segments (courtesy S. Esposito)

7.5.4.2.6 CCD

On a CCD with 4000*4000 pixels with a total size of 50*50 mm^2 one edge of a segment is sampled by approximately 40 pizels, while the typical signal obtained with one of the sensors is sampled by approximately 10 pixels perpendicular to the edge. Such a sampling is sufficient for an anlysis of the signals. Each pixel corresponds to a surface of 625 mm^2 on M1 and receives 10000 photons for typical integration times of 30 seconds, a bandwidth of 50 nm and reference star of magnitude 10.

Non-adaptive wavefront control

7.5.4.3 Open loop performance

To derive the information about the phase error from the signal delivered by a phasing sensor, different techniques can be used. The next section shows an example of a signal retrieval algorithm applied to the signal obtained in the laboratory with one of the sensors described above: the phase filtering technique.

7.5.4.3.1 The optical signal

The information about the phase step between two adjacent segments is recorded in an output signal which is localized at the intersegment border. The analytical expression for the signal, without taking into account the effects of atmospheric disturbances, is given by:

$$S = - \left(1 - f(b|x|)\right) \left\{ \underbrace{f(b|x|)\left(1 - \cos(\varphi_0)\right)\left(1 - \cos(\Delta\varphi)\right)}_{\substack{term \ 1 \\ symmetric}} - \underbrace{sign(x)\sin(\varphi_0)\sin(\Delta\varphi)}_{\substack{term \ 2 \\ anti-symmetric}} \right\} \qquad Eq. \ 7\text{-}1,$$

where *x* is a coordinate perpendicular to the border, with the origin x=0 on the border, $\Delta\varphi$ is a phase difference between two segments, φ_0 is a phase shift on the phase plate, *b* is parameter related to the diameter of the plate and the wavelength by $b = 0.6\pi a/\lambda$, and the function $f(bx)$ is the normalized sine integral. To take into account the smoothing of the signal due to atmospheric disturbances the Gaussian probability function can be used instead of sine integral. Therefore two types functions are used in the analysis for the signals:

$$f(bx) = \frac{2b}{\pi}\int_0^x \frac{\sin(bx')}{bx'}dx' \quad or \quad f(bx) = \frac{2b}{\sqrt{\pi}}\int_0^x \exp\left(-b^2x'^2\right)dx' \qquad Eq. \ 7\text{-}2$$

7.5.4.3.2 The CCD images

The reflective piston plate used for the laboratory test had hexagonal subapertures and different steps as shown in Figure 7-32:
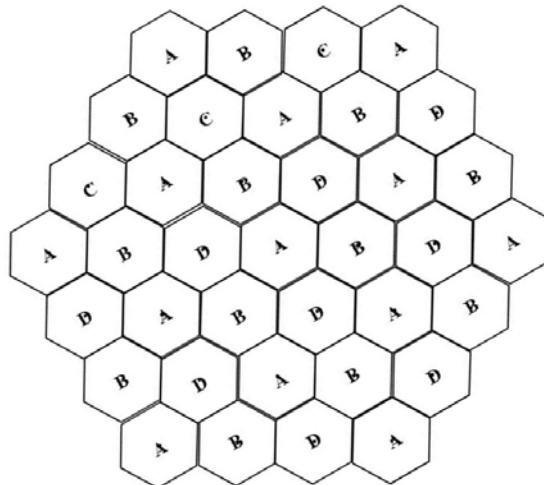

Figure 7-32. Position and surface piston levels of the hexagonal subapertures on the piston plate used for the laboratory tests (A=0nm, B=18nm, C=50nm, D=325nm).

The CCD image in Figure 7-33, shows for the two cases without and with turbulence in the optical path (seeing 0.36") shows a strong difference in the contrast.

Non-adaptive wavefront control
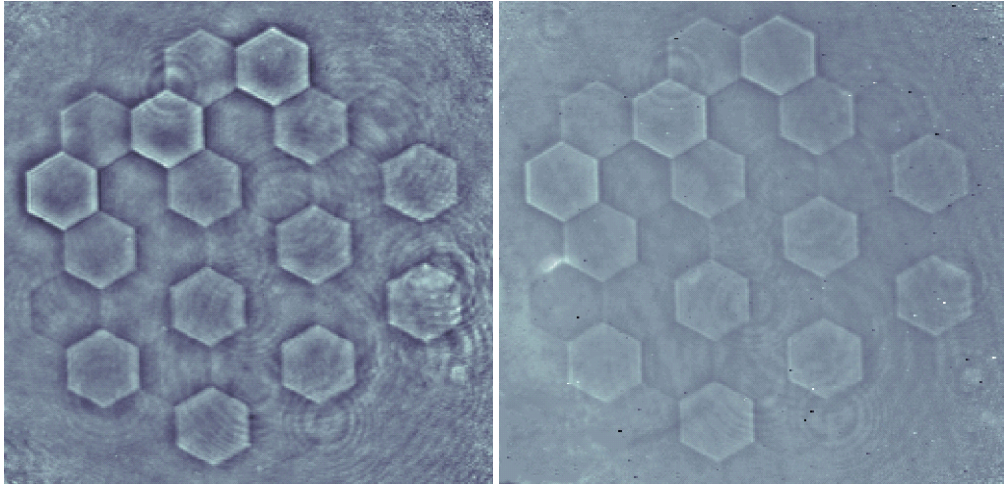
Figure 7-33. Phasing sensor signal from the multisegment phase plate without (left) and with (right) turbulence.

7.5.4.3.3 Signal analysis

To make full use of the knowledge about the analytical shape of the signal a fitting approach has been chosen for the signal analysis. Based on analytical expressions the following function has been fitted to the data:

$$S(x) = a_1 - \left[1 - f\left(a_4|x-a_3|\right)\right]\left[f\left(a_4|x-a_3|\right)\left(1-\cos(\varphi_0)\right)\left(1\pm\sqrt{1-a_2{}^2}\right) - a_2 \cdot sign(x-a_3)\sin(\varphi_0)\right] \qquad Eq.\ 7\text{-}3,$$

where the fitted parameters are: a_1 - constant background; a_2 - amplitude which is proportional to $\sin(\Delta\varphi)$, where $\Delta\varphi$ is the phase of the piston step; a_3 - shift of the edge with respect to the border; a_4 – parameter defined by the filter diameter.

The profile of the signal together with the fitted curve are shown for one of the borders in Figure 7-34 for two cases without (upper plot) and with (lower plot) the effects of atmospheric turbulence.
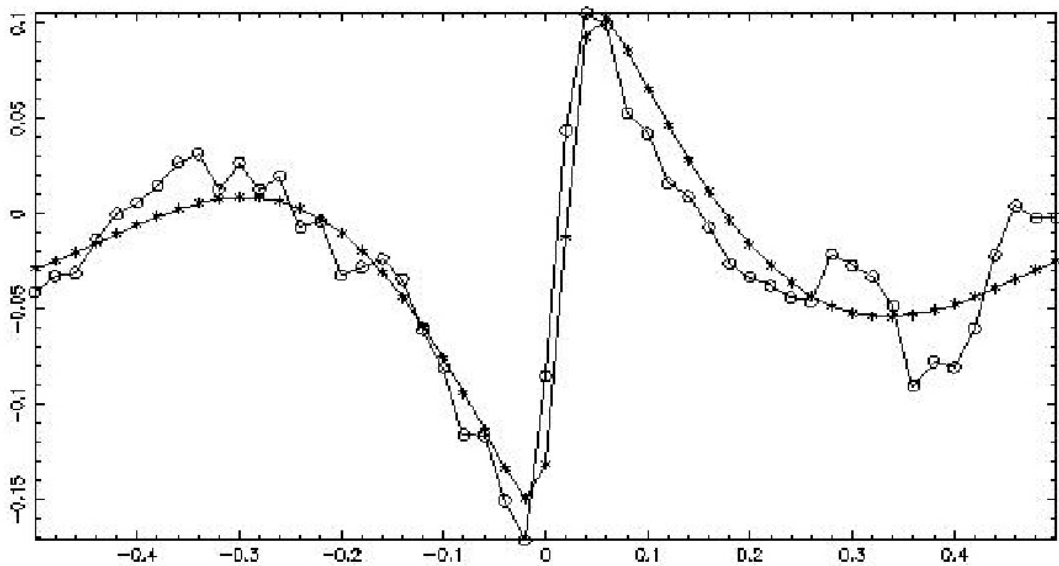
Figure 7-34. Sensor signals and fitted curves for one border for the two cases without (upper plot) and with (lower plot) turbulence. Note the change of the character of the signal : from an oscillating behaviour to smooth wings according to the function f.

7.5.4.3.4   Results

The fitting procedure was applied to the signals from all borders. Figure 7-35 shows for two measurements without and with a turbulence generator plots of the fitted amplitudes a_2 versus the piston steps known from the specifications for the piston plate. The solid lines represent sine curves with an amplitude C fitted to the data in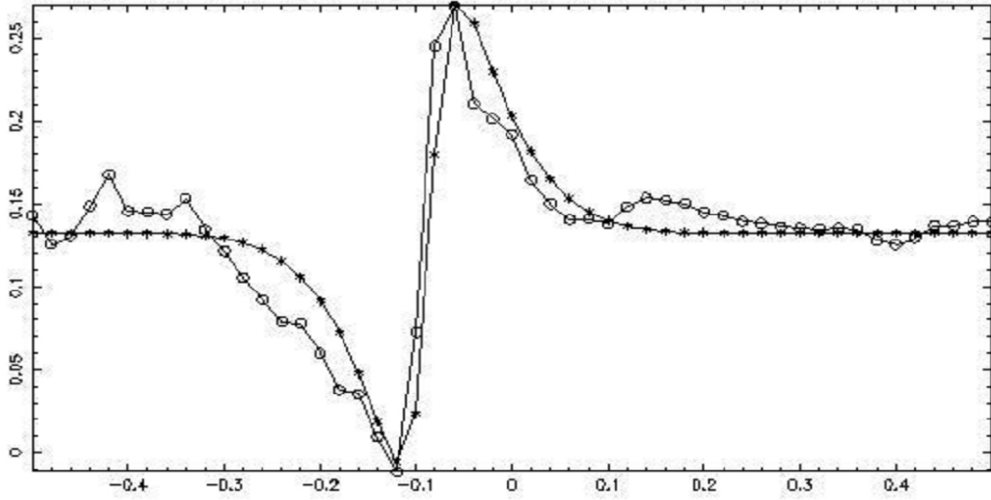 the plots. The RMS errors of the measurements can be obtained from the scatter of the measured data around the sine curves. They are 17 nm for the measurements without and 19 nm for the measurements with the turbulence generator. The small difference between the RMS values indicates that the scatter is not strongly dependent on the turbulence but rather defined by other sources of noise. The parameter C depends on the value of the seeing introduced by the turbulence. For the case without turbulence parameter C was found to be 0.65 which is in good agreement with the theoretically expected value of 0.7. A seeing of 0.6 arcseconds reduces the parameter C to 0.29. The atmospheric turbulence reduces the amplitude of the sine curve, but does not shift it. The determination of this parameter as a function of atmospheric seeing from calibrations or from theory is essential for the choice of the closed-loop gain.
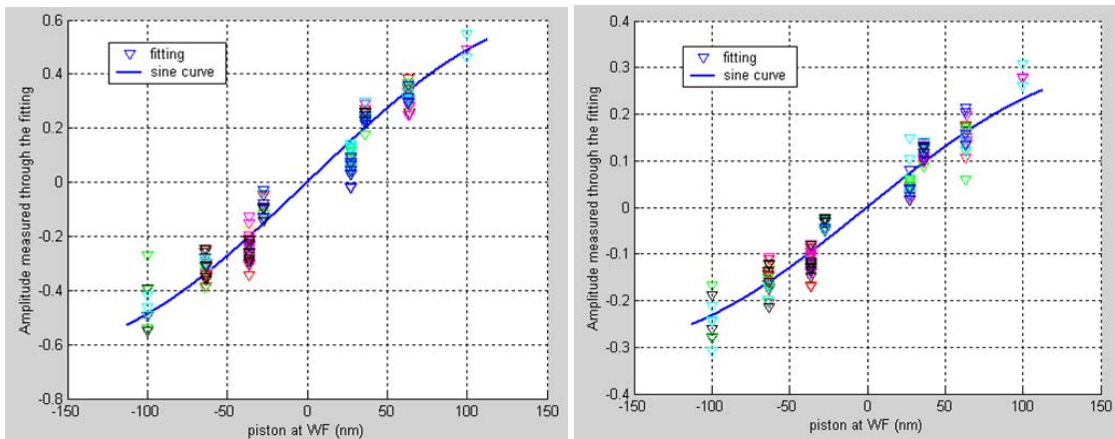

Figure 7-35. ZEUS measurements: amplitude of te signals versus known piston steps without (a) and with a turbulent generator (b). Note the reduction of the amplitude of the fitted sine curve from 0.65 to 0.29.

7.5.4.3.5   Increase of the capture range

Before optical phasing the misalignment of the segments can be several micrometers, whereas the capture range for measurements with quasi-monochromatic light is limited to $\lambda/2$. Methods for unwrapping the phase using multiple wavelengths techniques have been developed for interferometry [98].

The capture range is defined by two factors, namely the wavelengths and the measurement error, with the latter being the major limiting factor. Neverleless, for the small measurement errors of less than 10 nm the capture range is critically sensitive to the set of the chosen wavelengths. Even a small change in a wavelength can considerably affect the results.

7.5.4.3.6   Calibration

The algorithm for the reconstruction of the piston steps requires the knowledge of the parameter *C*. In the previous section *C* was determined by fitting a sine curve to measured data with a priori known abscissa values. In practice, *C* is an unknown parameter which has to be defined by calibrations or theory. To obtain the parameter C from a calibration procedure with well defined piston steps have to be introduced and the response of the sensors measured. Strictly speaking, the response of a sensor is not a symmetrical sine function centered on the origin as assumed above in the analysis of the experimental data, but rather a de-centered function:

$$a_2 = C\sin(\Delta\varphi + \varphi_1) + B \qquad\qquad Eq. \ 7\text{-}4,$$

where φ_1, *B* and the previously introduced parameter *C* depend in a random fashion on many external factors such as the non uniformity of the illumination, the system alignment, gaps, the quality of the segment edges, etc. For example, a difference in the edge profiles of two adjacent segments increases the parameter φ_1. This parameter is important for the final phasing precision: the iterative algorithm will converge to φ_1 instead of zero, unless this parameter is known from the calibration. As the calibration implies initially phased segments, the calibration of 3000 OWL segments on the sky is a time consuming task. The foreseen base-line is the use of pre-calibrations. The static aberrations of the segments, including the aberrations at the edges, are the most severe sources for phasing errors. These factors have to be taken into account at the level of the surface maps of the segments. The influence of the parameter *C* due to, for example, a change of the seeing during the operation can be taken into account by an appropriate tuning of the gain in the closed-loop control.
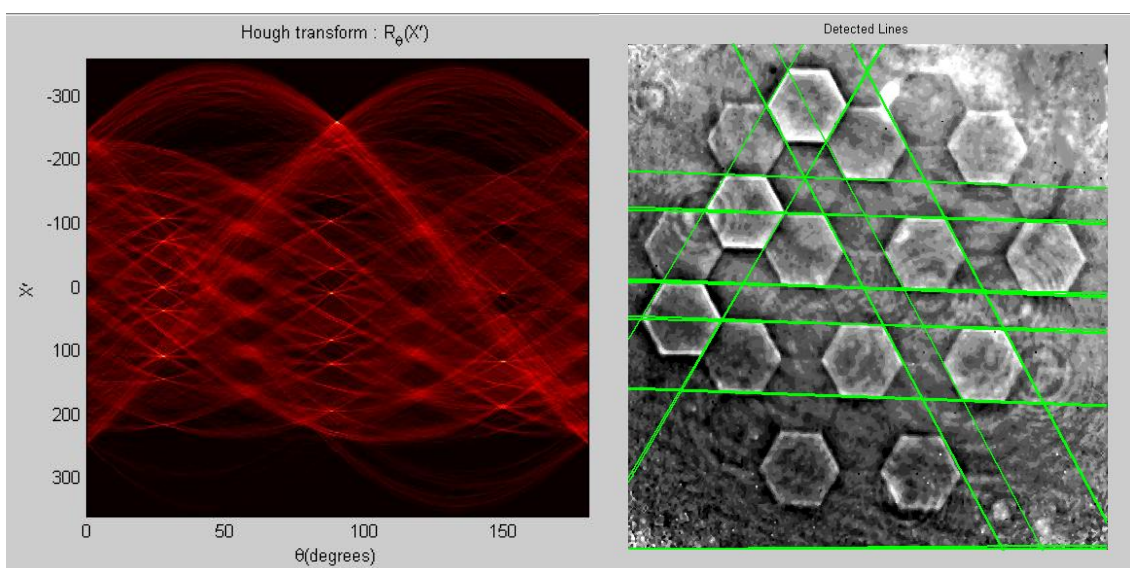

Figure 7-36. Hough transform of the signal (left) and the detected lines (right).

7.5.4.4 Identification of the borders

The algorithms described above require the determination of the location of the intersegment borders on the CCD with a precision better than one pixel. The Hough transform is a suitable algorithm to detect lines, circles, ellipses or other figures which have a known functional description. Before applying it to an image, the contrast in the image should be increased via the Sobel operator, which performs a 2-D spatial gradient measurement on an image and thereby emphasizes regions of high spatial frequency expected at the borders between segments. Figure 7-36 shows the application of the Sobel and Hough transforms to an image obtained with the phase filtering sensor.

7.5.4.5 Closed-loop results

A fitting technique has been implemented for measuring the piston steps between neighbouring segments in a segmented mirror. For the correction of the piston steps one needs the relationship between the piston movements of all of the segments and the resulting piston steps at all intersegment borders. This is given by a system of linar equations $\mathbf{Ax} = \mathbf{b}$, where $\mathbf{A}$ is a matrix, $\mathbf{x}$ a vector containing the piston movements, and $\mathbf{b}$ a vector containing the piston steps. The matrix $\mathbf{A}$ is a sparse matrix consisting only of of values -1, 0, 1 and can be calculated analytically from the geometry of the mirror. The control matrix $\mathbf{B}$, which calculates the piston movements from the measured piston steps is the inverse of $\mathbf{A}$, obtained by singular value decomposition (SVD). Since the system equation is over-determined, as there more borders than segments, the method automatically provides a best fit in the least square sense of the piston movements to the piston steps and thereby reduces the error. The only piston error which can not be detected and corrected by this method is a global piston movement of the mirror.
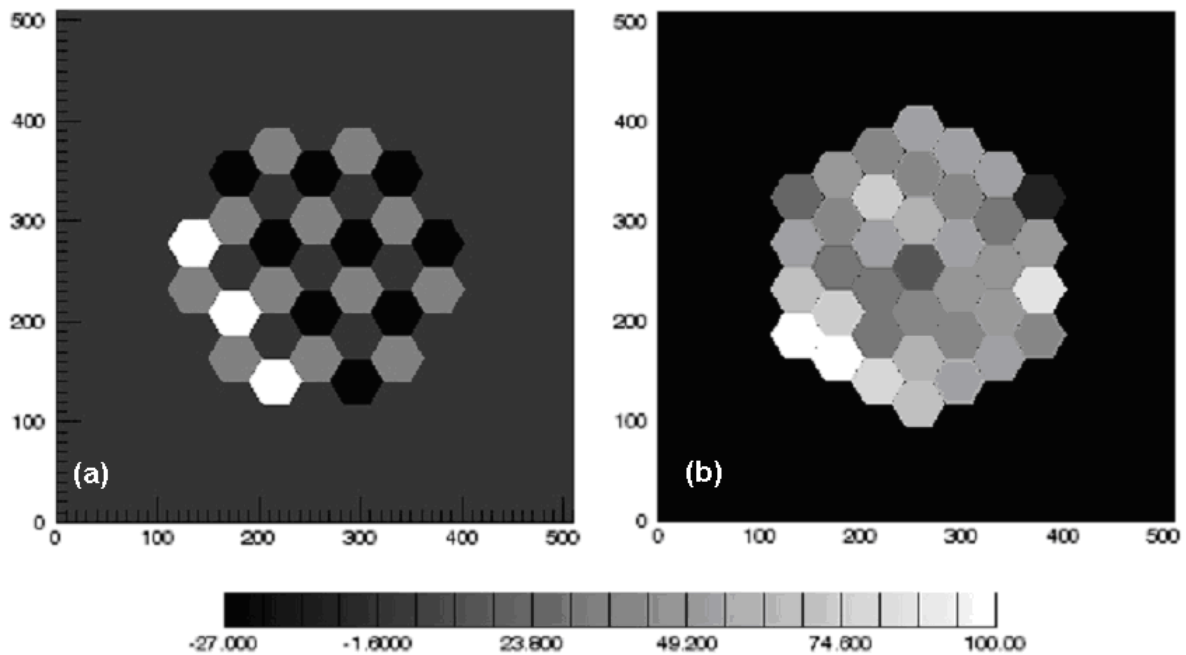
Figure 7-37. Piston steps distribution: Initial (a) and after 6th loop (b). The grey scale is in nm.

For a simulation of the closed-loop behaviour a segmented mirror has been generated with the same characteristics of the piston plate as the one used in the laboratory experiment (Figure 7-37 on the left hand side). Atmospheric turbulence has been simulated by using the phase screen corresponding to a seeing of 0.6", moving with a wind speed of 5m/s. The integration time for each measurement was 2 sec. Readout noise and the photon noise corresponding to a relatively bright star of magnitude 6 have also been included. Figure 7-37 shows on the right hand side the distribution of the phase errors after the 6th iteration. Figure 7-38 shows the convergence of the residual RMS error with the iterations using a gain of 0.5.
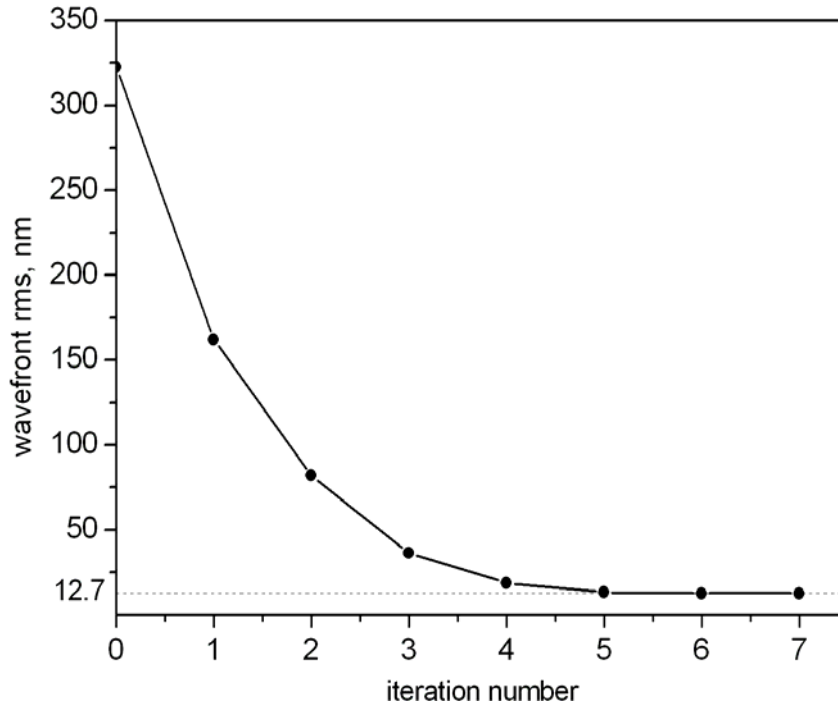
Figure 7-38. Closed loop simulations. Gain 0.5.
Initial wave front RMS = 322.5nm, final RMS = 12.7nm.

7.5.4.6   Phasing OWL

Owing to the obscuration by to the support structure of the M2 unit the primary mirror is, at least as seen by the phasing wavefront sensors, divided into six separate petals. Information about the piston steps between neighbouring segments can therefore only be supplied by the optical wavefront sensors for edges within a petal, and only individual petals can be phased with the matrix method desribed in the previous section. In a second stage the petals themselves have to be phased with respect to each other.

7.5.4.6.1   Phasing of one petal

The primary mirror of OWL has 2964 segments plus 54 segments obscured by the support of M2. In one petal alone one still needs to phase 494 segments having 1398 inter-segment borders. Therefore the matrix **A** mentioned above has 494x1398 = 690612 elements. Fortunately, this matrix is sparse to high degree. By using a specific indexation the matrix can be written in block-diagonal form. One can then apply matrix algebra techniques for sparse matrices and reduce the time for a SVD. This could be particularly useful if the matrix **A** changes during the operation because of a failure of edge sensors. Figure 7-40 shows the proposed indexation of segments and borders.
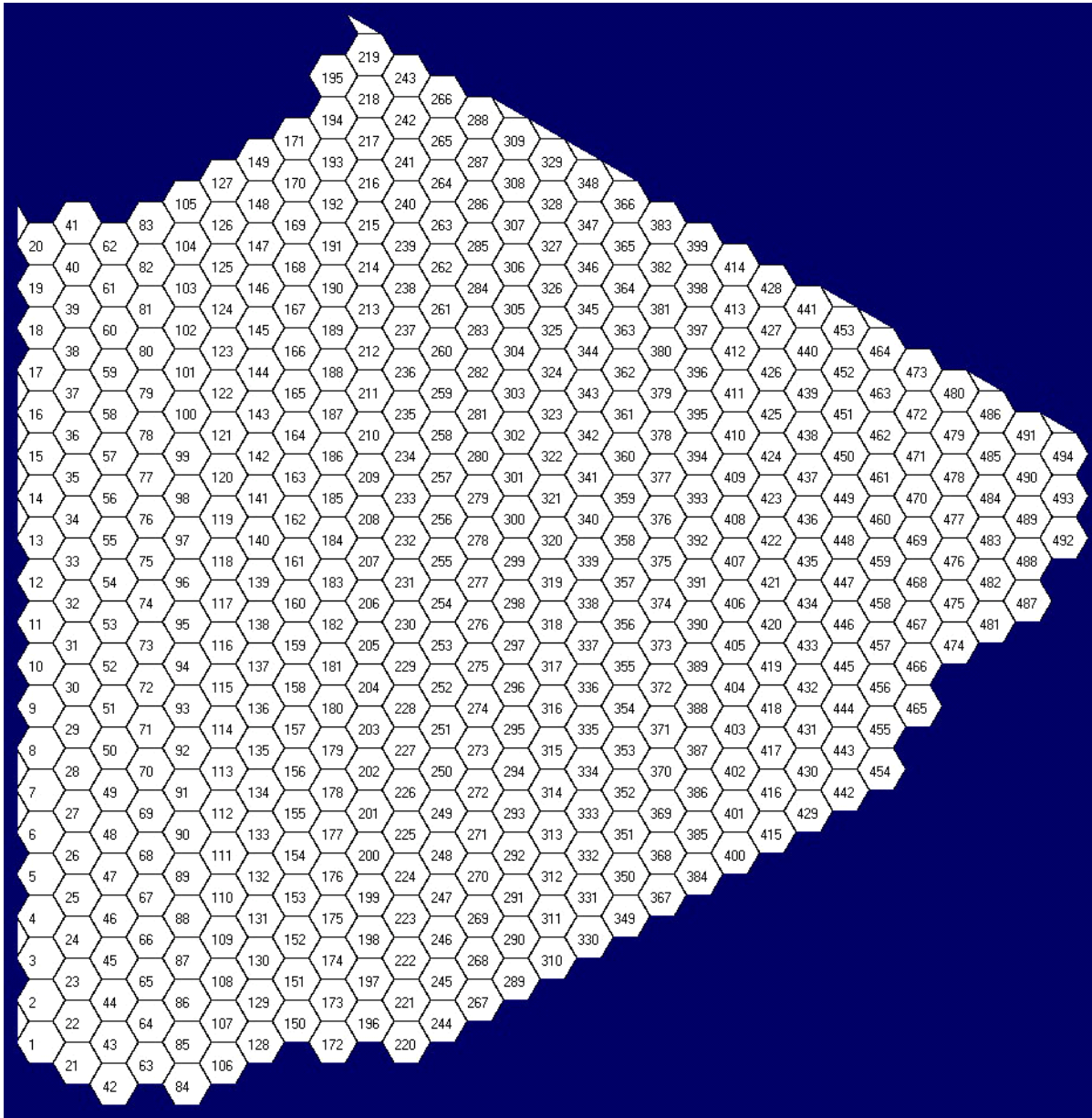
Figure 7-39 Indexation of the segments
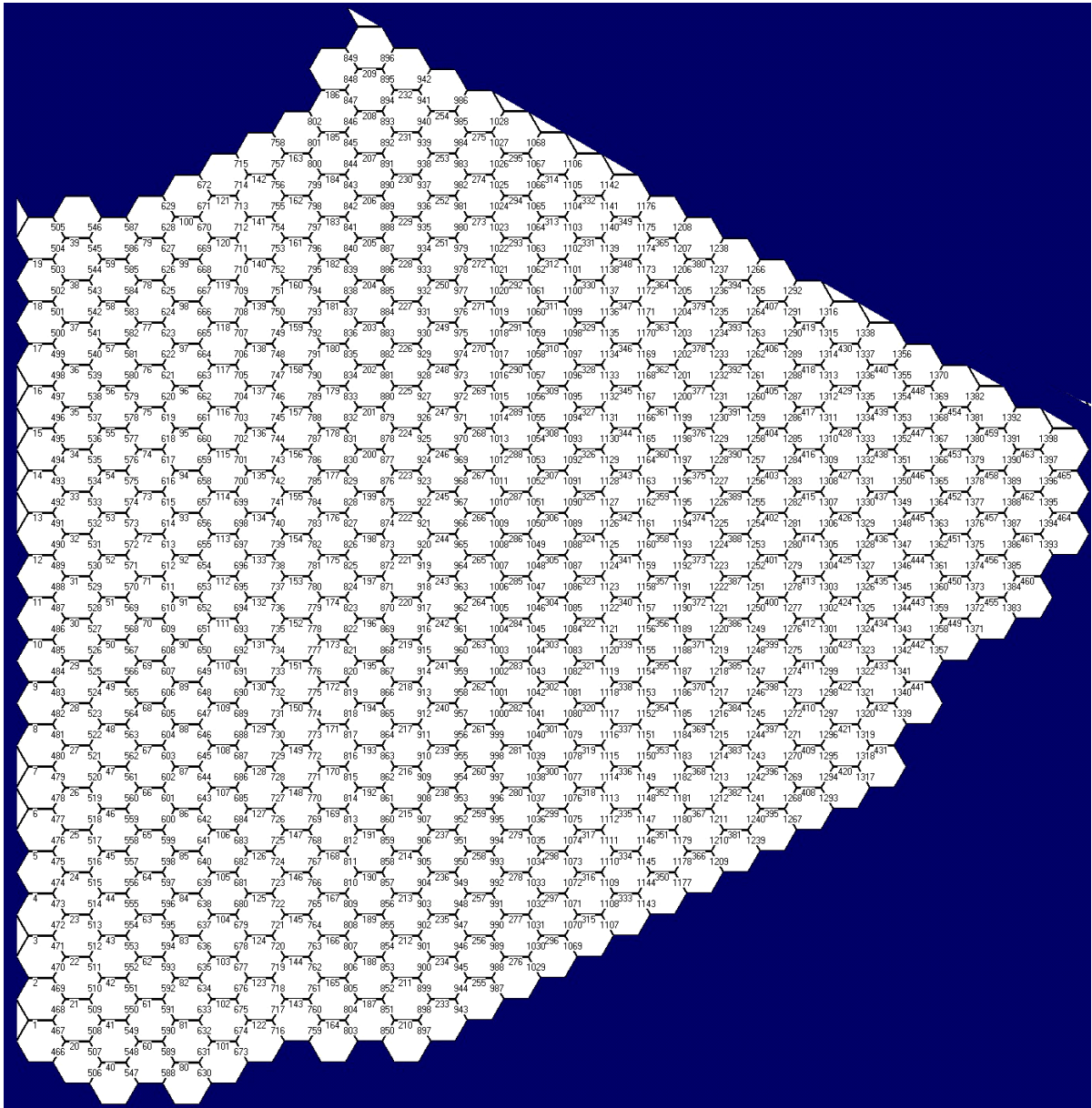
Figure 7-40. Indexation of the borders between the segments

This indexation allows writing the iteration matrix in a block form:

$$A = \begin{bmatrix} Q \\ P \end{bmatrix}$$

where Q and P are also block matrices of dimension 29x29 (diagonal and quasi diagonal):

$$Q = \begin{bmatrix} Q_{11} & & & 0 \\ & \ddots & & \\ & & \ddots & \\ 0 & & & Q_{29\,29} \end{bmatrix} \qquad P = \begin{bmatrix} -P_{11} & P_{12} & & & 0 \\ & \ddots & & \ddots & \\ 0 & & & -P_{28\,28} & P_{28\,29} \end{bmatrix}$$

The elements in the diagonal of the first matrix are 29 matrixes of the same type B_n :

$$[\mathbf{Q}_{11} \; ... \; \mathbf{Q}_{2929}]=$$

$$=[\; \mathbf{B}_{20} \;\; \mathbf{B}_{21} \;\; \mathbf{B}_{21} \;\; \mathbf{B}_{21} \;\; \mathbf{B}_{22} \;\; \mathbf{B}_{22} \;\; \mathbf{B}_{22} \;\; \mathbf{B}_{22} \;\; \mathbf{B}_{24} \;\; \mathbf{B}_{24} \;\; \mathbf{B}_{24} \;\; \mathbf{B}_{23} \;\; \mathbf{B}_{22} \;\; \mathbf{B}_{21} \;\; \mathbf{B}_{20}...$$

$$...\mathbf{B}_{19} \;\; \mathbf{B}_{18} \;\; \mathbf{B}_{17} \;\; \mathbf{B}_{16} \;\; \mathbf{B}_{15} \;\; \mathbf{B}_{14} \;\; \mathbf{B}_{13} \;\; \mathbf{B}_{12} \;\; \mathbf{B}_{11} \;\; \mathbf{B}_{9} \;\; \mathbf{B}_{7} \;\; \mathbf{B}_{6} \;\; \mathbf{B}_{5} \;\; \mathbf{B}_{3} \;]$$

The elements of the matrix P are quasi diagonal matrices of several types:

$$[\mathbf{P}_{11} \; ... \; \mathbf{P}_{2828}]=$$

$$[\mathbf{C}_{20} \;\; \mathbf{E}_{21} \;\; \mathbf{D}_{21} \;\; \mathbf{C}_{21} \;\; \mathbf{D}_{22} \;\; \mathbf{D}_{22} \;\; \mathbf{D}_{22} \;\; \mathbf{C}_{22} \;\; \mathbf{D}_{24} \;\; \mathbf{E}_{24} \;\; \mathbf{F}_{24} \;\; \mathbf{F}_{23} \;\; \mathbf{F}_{22} \;\; \mathbf{F}_{21} \; ...$$
$$...\mathbf{F}_{20} \;\; \mathbf{F}_{19} \;\; \mathbf{F}_{18} \;\; \mathbf{F}_{17} \;\; \mathbf{F}_{16} \;\; \mathbf{F}_{15} \;\; \mathbf{F}_{14} \;\; \mathbf{F}_{13} \;\; \mathbf{F}_{12} \;\; \mathbf{F}_{11}^{-} \;\; \mathbf{F}_{9}^{-} \;\; \mathbf{F}_{7}^{-} \;\; \mathbf{F}_{6}^{-} \;\; \mathbf{F}_{5}^{-} \;]$$

$$[\mathbf{P}_{12} \; ... \; \mathbf{P}_{2829}]=$$

$$[\mathbf{F}_{21} \;\; \mathbf{D}_{21} \;\; \mathbf{E}_{21} \;\; \mathbf{F}_{22} \;\; \mathbf{E}_{22} \;\; \mathbf{E}_{22} \;\; \mathbf{E}_{22} \;\; \mathbf{F}_{24}^{+} \;\; \mathbf{E}_{24} \;\; \mathbf{D}_{24} \;\; \mathbf{C}_{23} \;\; \mathbf{C}_{22} \;\; \mathbf{C}_{21} \;\; \mathbf{C}_{20} \; ...$$
$$...\mathbf{C}_{19} \;\; \mathbf{C}_{18} \;\; \mathbf{C}_{17} \;\; \mathbf{C}_{16} \;\; \mathbf{C}_{15} \;\; \mathbf{C}_{14} \;\; \mathbf{C}_{13} \;\; \mathbf{C}_{12} \;\; \mathbf{C}_{11} \;\; \mathbf{C}_{9} \;\; \mathbf{C}_{7} \;\; \mathbf{C}_{6} \;\; \mathbf{C}_{5} \;\; \mathbf{C}_{3} \;]$$

where $\mathbf{B}_n$, $\mathbf{C}_n$, $\mathbf{D}_n$, $\mathbf{E}_n$, $\mathbf{F}_n$, $\mathbf{F}_n^{+}$ $\mathbf{F}_n^{-}$ are block-matrixes consisting of values 1, -1 and 0 with corresponding dimensions [n-1, n], [$2n$, n], [$2n$-1, n], [$2n$-1, n], [$2n$-2, n], [$2n$-4, n], [$2n$-4, n]:

$$\mathbf{B}_n = {\begin{matrix} & 1 & & & n \\ 1 \\ & \\ n-1 \end{matrix}}\begin{bmatrix} 1 & -1 & & & 0 \\ & 1 & -1 & & \\ & & \ddots & \ddots & \\ 0 & & & 1 & -1 \end{bmatrix}$$

$$\mathbf{C}_n = {\begin{matrix} & 1 & & n \\ 1 \\ \\ \\ 2n \end{matrix}}\begin{bmatrix} 1 & & 0 \\ 1 & & \\ & 1 & \\ & 1 & \\ & \ddots & \\ & \ddots & \\ & & 1 \\ 0 & & 1 \end{bmatrix}$$

$$\mathbf{D}_n = {\begin{matrix} & 1 & & n \\ 1 \\ \\ \\ 2n-1 \end{matrix}}\begin{bmatrix} 1 & & 0 \\ 0 & 1 & \\ & 1 & \\ & \ddots & \\ & \ddots & \\ & & 1 \\ 0 & & 1 \end{bmatrix}$$

$$\mathbf{E}_n = {\begin{matrix} & 1 & & n \\ 1 \\ \\ \\ \\ \\ 2n-1 \end{matrix}}\begin{bmatrix} 1 & & 0 \\ 1 & & \\ & \ddots & \\ & \ddots & \\ & & 1 \\ & 1 & 0 \\ 0 & & 1 \end{bmatrix}$$

$$\mathbf{F}_n = {\begin{matrix} & 1 & & n \\ 1 \\ \\ \\ \\ \\ 2n-2 \end{matrix}}\begin{bmatrix} 1 & & \\ 0 & & 0 \\ 1 & & \\ 1 & & \\ & \ddots & \\ & & 1 \\ 0 & & 1 & 0 \\ & & & 1 \end{bmatrix}$$

$$
\boldsymbol{F}_n^{+} =
\begin{array}{c}
 \\
1 \\
 \\
 \\
 \\
 \\
 \\
 \\
2n-4
\end{array}
\overset{\displaystyle 1 \qquad\qquad\qquad n}{
\begin{bmatrix}
1 & & & & & & \\
 & 1 & & & 0 & & \\
 & 1 & & & & & \\
 & & & \ddots & & & \\
 & & & & 1 & & \\
0 & & & & 1 & & \\
 & & & & 1 & 0 &
\end{bmatrix}}
\qquad
\boldsymbol{F}_n^{-} =
\begin{array}{c}
 \\
1 \\
 \\
 \\
 \\
 \\
 \\
 \\
2n-4
\end{array}
\overset{\displaystyle 1 \qquad\qquad\qquad n}{
\begin{bmatrix}
0 & 1 & & & & & \\
 & & 1 & & 0 & & \\
 & & 1 & & & & \\
 & & & \ddots & & & \\
0 & & & & 1 & & \\
 & & & & 1 & & \\
 & & & & & & 1
\end{bmatrix}}
$$

7.5.4.6.2 Phasing of the petals

Six petals separated by secondary support obscuration may be considered as 6 large segments provided that all segments within each petal are aligned. For the phasing petals one could follow the same strategy as applied to the phasing of the segments. However, because of the small number of elements also other techniques may be implemented.

Two techniques are considered at the moment. The first one is based on the Shack-Hartmann method with two lenslets along each dividing line between two petals and centered on this line. The size of each of the 12 lenslets would correspond to a subaperture of approximately 12 m on M1. The principle of this measurement is the same as for the Shack-Hartmann sensor used for the phasing of segments described above.

The second method is a "dispersed - speckles" technique developed by A. Labeyrie for piston sensing in hypertelescopes with a densified exit-pupil. The method is based on an analysis of the image formed by multiple apertures and the extraction of the information about the piston errors from the structure of the speckle image [99].

7.5.4.6.3 Measurements under aberrations

Some types of sensors may be sensitive to other aberrations introduced by the telescope. These aberrations can be regarded as noise added to the piston sensing system, which reduces the resolution of the sensor. This may be a problem for the precision of the phasing if stars are chosen in the technical field which will be affected by field aberrations. The possible procedures for the alignment of the telescope based on measurements in the field have to take this feature into account.

7.5.4.6.4 Disentangling M1&M2

The precise determination of the positions of the mirrors in the image on the CCD is one of the critical points of the signal analysis. Besides, the signals from two segmented patterns (primary and secondary mirrors) overlap. As the two segmented pattern have different spatial scales, the signal can be disentangled using a Fourier filtering. To image the mirror gaps, a high pass filter is applied in the focal plane. It can be realized as the coronagraphic absorbing mask with a diameter of approximately 40-50 λ/D. In the next pupil plane the gaps appear as bright lines, corresponding to two segmentation grids (Figure 7-41). Then the Fourier filtering is applied with the spatial frequencies corresponding to the two patterns (Figure 7-41). The size of each spot is 2λ/D. Fourier filtering can be implemented in the software or by optical devices. After the filtering one or the other of the two segmentation pattern will be revealed (Figure 7-41 c, d).
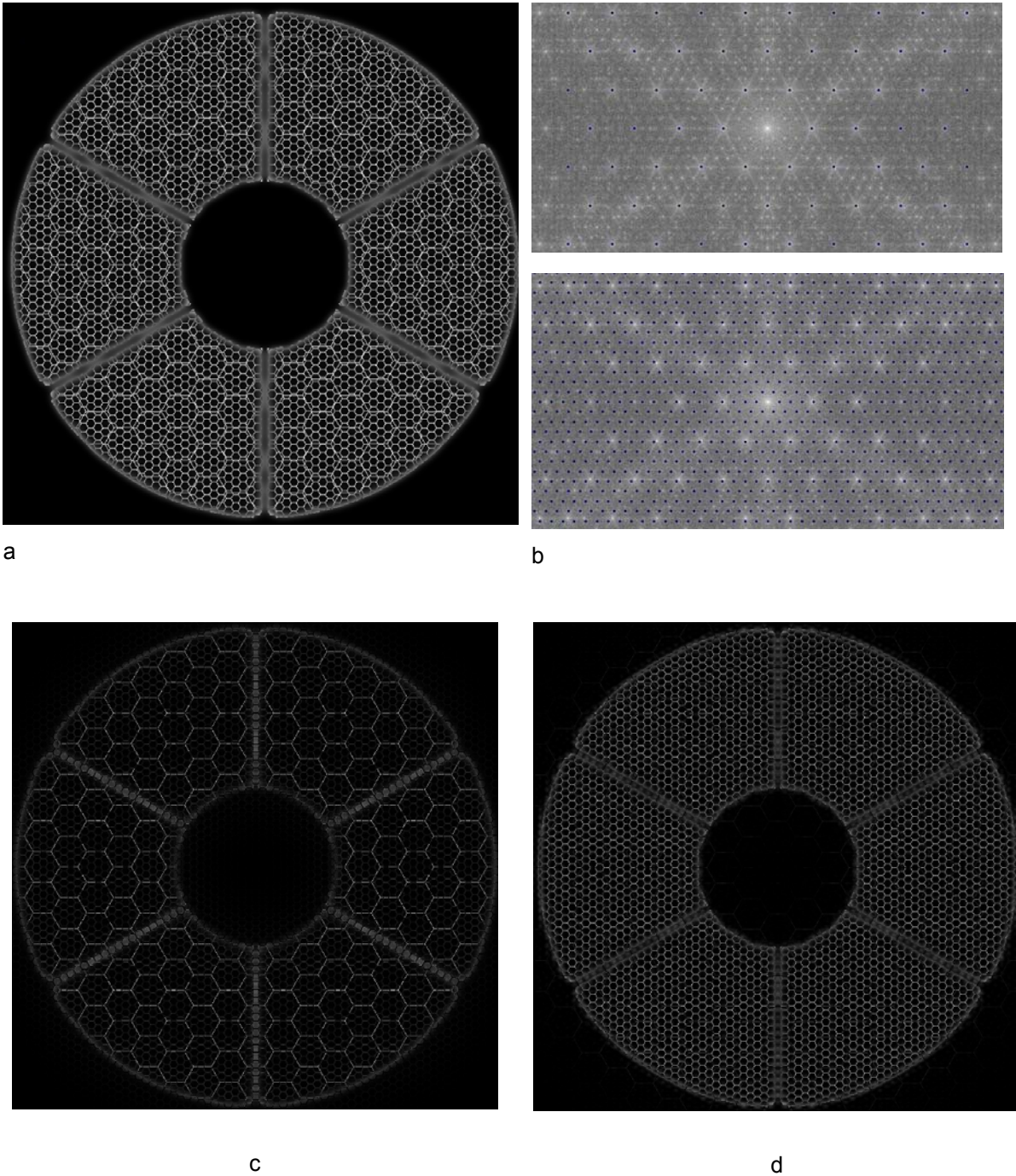
a

b

c

d

Figure 7-41. The signal from the gaps obtained by a high-pass filtering (a),
two spatial Fourier filters (b), and the filtered patterns for the secondary (c) and primary (d) mirrors.

7.5.5   Control of segmented mirrors (M1 & M2)

To achieve the required optical performance, each segment should be positioned relative to adjacent segments with an accuracy of a few nanometers. In this section the segments are considered to be rigid bodies. Any wavefront aberrations due to segmentation are then introduced purely by deformations of the support structure of the segmented mirrors. At low temporal frequencies such deformations can be generated gravitationally by changes of the telescope altitude angle or by the effects of thermal variations. At higher temporal frequencies the major disturbance is the wind affecting the overall support structure and the individual segments.

Non-adaptive wavefront control

A closed-loop control of the segment positions has to reduce these wavefront aberrations. The information about the discontinuities at the segment interfaces is obtained from two types of sensors: first, capacitive or inductive edge sensors and, second, optical wavefront sensors which generate the references for the first type of sensors. The corrections are done by position actuators, which can correct each segment position in three degrees of freedom. A control algorithm based on the measurements generates the command for the actuators.

The problem of segment control has extensively been studied by the Keck and CELT ([26], [27]) projects. The approach consists of two major steps. First, the required displacements for each actuator are estimated from the data obtained by the edge sensors with the help of a control matrix which has been obtained by inverting the influence matrix with singular value decomposition, and, second, an integral control law is used for the application of the corrections. The use of the integral control law is justified by the assumptions that the control is used only for correcting the slow perturbations generated by load and temperature variations, and that a low bandwidth control is sufficient. However, with faster perturbations due to wind buffetting, low bandwidth control system using proportional integral control would not necessarily deliver the required performance in the case of OWL. Hence, control laws with a higher bandwidth and better performance taking into account the dynamic behaviour of segments should be designed.

To develop a control strategy for the phasing of the segmented mirrors affected by wind perturbations a step by step approach has been adopted. First, the control of a single segment considering a stiff backstructure has been studied. The goal was to understand to what extent the local control system can 'freeze' the segments against the wind load perturbation. The outcomes of such a study are the requirements on the control bandwidth, position actuators and noise of the edge sensors. In the next step the effect of the back structure has been studied. The telescope structure has been represented by its equivalent inertia and stiffness.
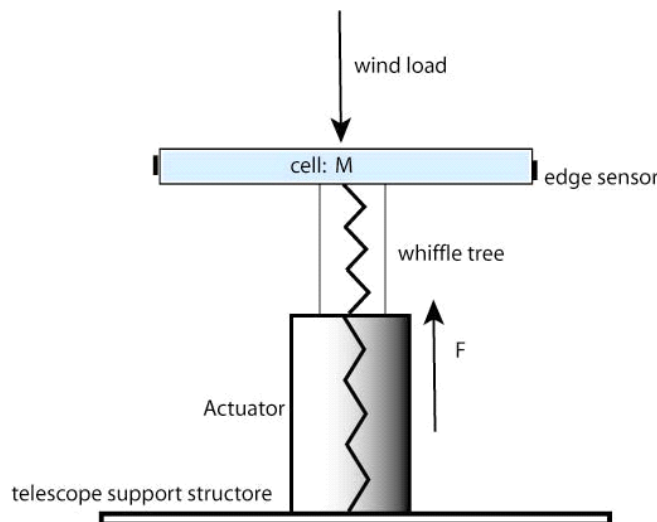

Figure 7-42 Scheme of segment system configuration

The wind load is characterized by a von Karman PSD, shown for a wind velocity of 10 m/s in Figure 7-43..

The control study for one segment has been extended to the case of a group of segments. First, the control of a ring of seven segments has been considered. The objective of the control has been to minimize the relative displacements between adjacent segments caused by wind perturbation. Two approaches for the control have been considered. In the first approach actuator movements are estimated via an inverted interaction matrix (the control matrix) from all edge sensor measurements. The correction is done in closed loop with a local controller. This approach is similar to the classical approach used in Keck, except for the design of the local controller. In the second approach the local controller for each segment uses only local information from the edge sensors around one segment. In this approach no inversion of an interaction matrix is needed. These issues will be discussed in more detail below.
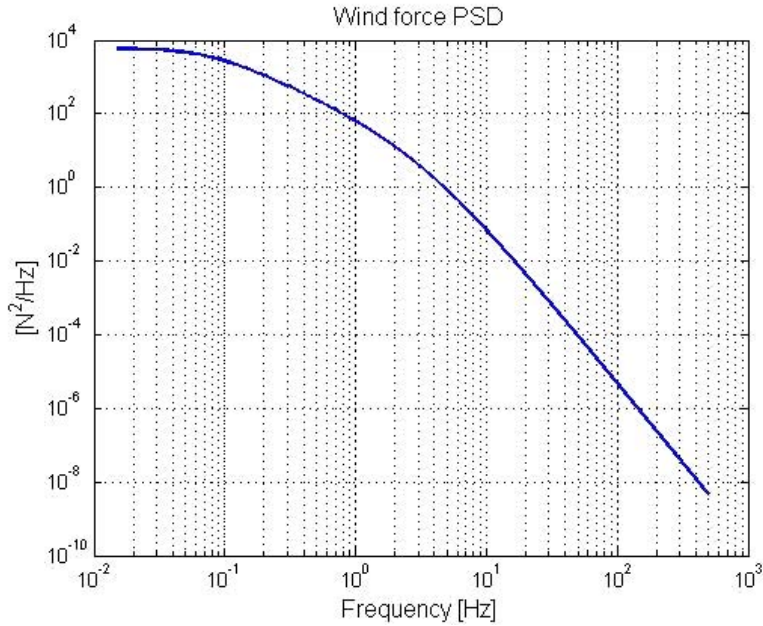
Figure 7-43 PSD of wind load on one segment

The study of the control of one segment is discussed in RD19. The mechanical description of the segment with a whiffle tree support system and three actuators is described in section 9.4.6. The dynamical model of the segment is given in RD20. The segment is modelled by a rigid body with three degrees of freedom and the whiffle tree system by a spring and a damper. The segment and the whiffle trees are connected to three actuators modelled by springs and the active forces that they can apply in response to the controller command. The complete system is subjected to an external wind load. A simplified scheme of a segment system is shown in Figure 7-42. Assuming a Zerodur mirror the weight of a segment is approximately 400 Kg. The frequency of the piston mode of the segment on its axial support system is expected to be at least 60 Hz and the structural damping on the whiffle tree system to be 1%.
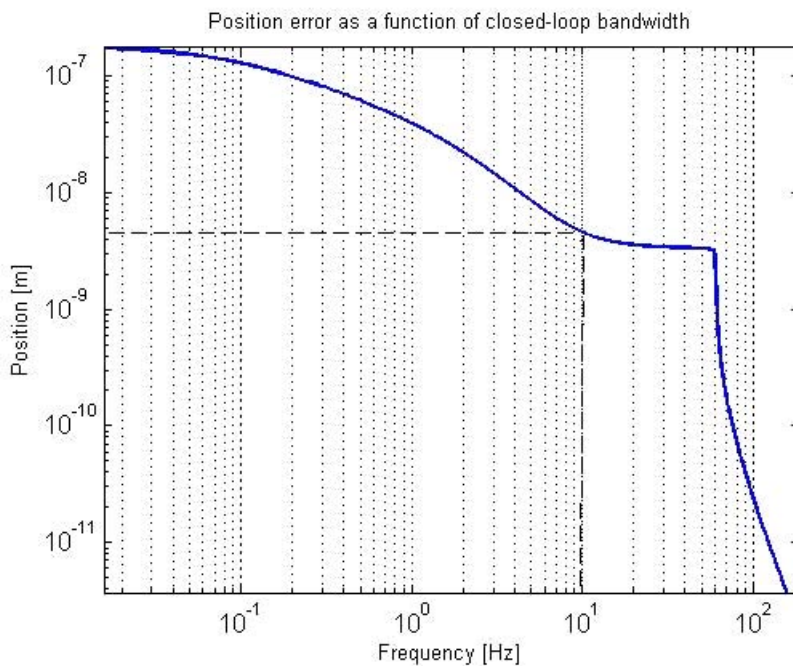
Figure 7-44 Position error RMS as a function of control bandwidth of each actuator

Non-adaptive wavefront control

The objective of the segment control is to freeze the absolute position of a segment subjected to wind perturbations with an expected accuracy requirement in the range of 5 nm RMS. To obtain an initial crude estimate for the required control bandwidth for each actuator, the RMS of the position error has been calculated as a function of the closed-loop bandwidth with perfect control actions, shown in Figure 7-44.

The required accuracy can be obtained with a control bandwidth of at least 10Hz. A controller has now been designed taking into account the characteristics of the perturbation and the dynamics of the segment. The parameterisation and the design procedure, which is based on loop-shaping, are discussed in RD19. The control bandwidth for each actuator is set to 10Hz. Figure 7-45, comparing the PSDs of the position of the segment under closed-loop and open-loop control, shows that the controller considerably improves the performance of the system.
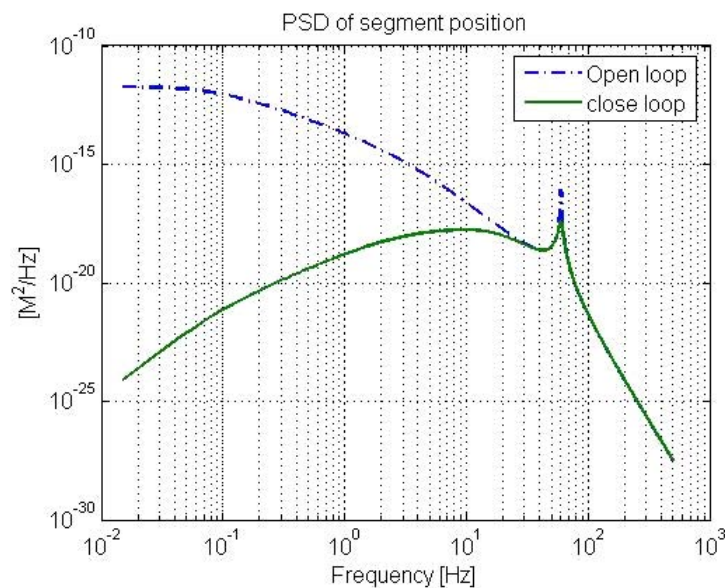
Figure 7-45 Closed-loop position error PSD compared to open loop PSD

The closed-loop performance has been verified by a simulation. The sensor noise was represented by a band-limited white noise with an amplitude of the spectral density of 0.7 nm/$\sqrt{Hz}$ [62] and has been introduced at the output, that is the absolute position of the segment. Sensor noise is usually amplified by the controller which consequently generates noisy input command to actuators. This can be avoided by installing a filter with a cut-off frequency higher than the control bandwidth after the output measurements. Figure 7-46 shows the results of the closed-loop simulation. The RMS error of segment position is 6.5 nm.

The rejection of the effects due to disturbances can be considerably improved if some prior information about the characteristics of the disturbances such as wind buffeting is available. This could be obtained by measuring the acceleration of segments which contains unfiltered information about the disturbing force at least for frequencies lower than the resonance frequency of the segment on its support. The control system will react faster to cancel out disturbances and the stringent requirement on the bandwidth of the position control can be relaxed. The results of a simulation of the position control of one segment with a control design including an acceleration feedback control (AFC), following the approach presented in [21], are shown in Figure 7-47.

The same position feedback controller has been used with the same parameters as in Figure 7-46.. Figure 7-47 shows that most of the correction the disturbance is done by the AFC part of the control, shown in red. This suggests that the desired performance can even be achieved using a position controller with a lower bandwidth. Figure 7-47 shows the simulation results

---

[62] Corresponding to 2 [nm] RMS sensor noise at 10Hz.

using the AFC and a position feedback control with a closed-loop bandwidth of 5 Hz for each actuator. The RMS error of the absolute position of a segment is now 4 nm as compared to 6.5 nm with the 10 Hz bandwidth without an AFC.
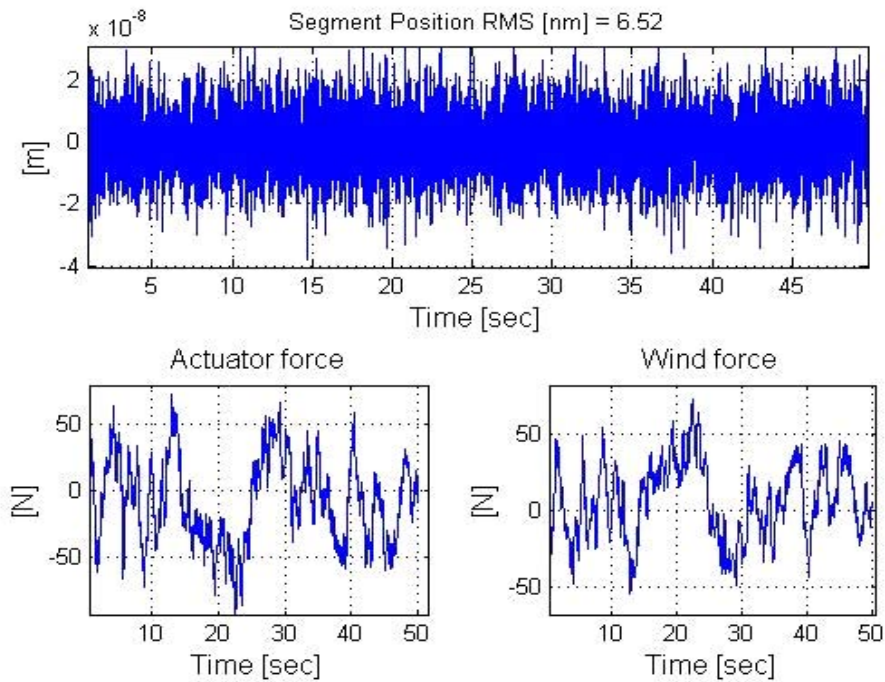
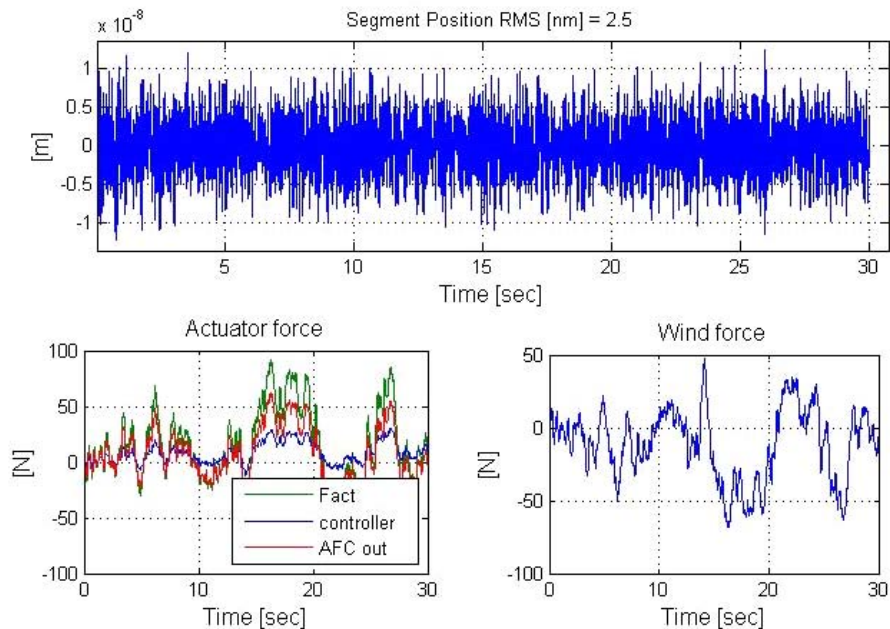Figure 7-46 Closed-loop response of system--- closed-loop bandwidth: 10Hz

Figure 7-47 Closed-loop simulation ---- with AFC, closed-loop bandwidth 10Hz

Currently studies related to the control of a group of segments are under way. The coupling issues, i.e. coupling between the actuator commands on one segment, coupling between segments, and the effect of the control on the support structure will be studied in detail. The effect of wind on the segments, the control strategy and the performance of the actuators and edge sensors will be investigated in detail in the framework of the ELT Design Study (see RD506, RD504, RD502).

Non-adaptive wavefront control

Some worry has been expressed that the control of segments at frequencies higher than the lowest frequencies of the telescope structure can generate resonances in the telescope structure. However, early studies have indicated that this is not the case for the control of the segments in segmented mirrors.
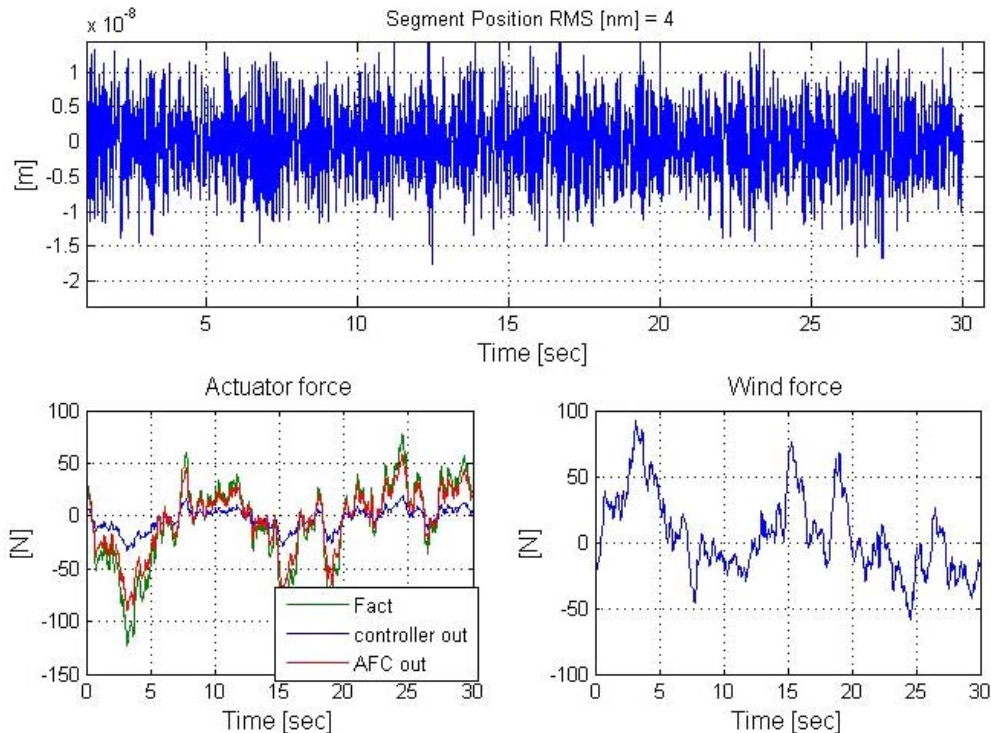
Figure 7-48 Closed-loop simulation ---- with AFC, closed-loop bandwidth 5Hz

The problem of controlling the segment can be decoupled from the dynamics of the support structure. The support structure will only be excited by wind perturbations and not by the actions of the control of the segments, regardless of the nature of the control and its bandwidth. The proof, which is given in RD19, is based on singular perturbation theory [24], [25]. The main idea behind the dynamic decoupling is the large separation between the time-scales related to the dynamics of the segments and the support structure. Since the natural frequency of 60 Hz of each segment unit is much larger than the lowest significant frequencies of 2.6 Hz of the telescope (see section 9.5.4.1), the system can dynamically be partitioned into to a fast subsystem, the segment control system, and slow subsystem, describing the dynamics of the support structure. The result of applying singular perturbation theory is that the only external force acting on the support structure is the perturbation due to the wind load.

The motion of the support structure caused by the wind will act as an external perturbation on the absolute position of a segment. This implies that a group of segments will move together with the back structure at low frequencies corresponding to the global modes of the structure.

To confirm the theoretical results, the telescope support structure has been modelled by an equivalent mass and a spring such that the lowest eigenfrequency of the telescope structure is 2.6 Hz. A simulation has been done for the closed-loop response of the segment system with a control bandwidth of 10Hz for each actuator. Figure 7-49 shows that the reaction force on the back structure is approximately equal to the wind force. The differences are comparatively small high frequency fluctuations around the time series of the wind load. The comparison between the PSDs of the wind and the reaction force, shown in Figure 7-50, also confirms that the wind load and the reaction force on the support structure have the same frequency content except at frequencies close to eigenfrequency of 60 Hz of the segment system.

Assuming a weak dynamical coupling between segments, the local controller for a single segment can also be used for the control of a group. The main difference between the control of a single and a group of segments is that the position errors are minimized relative to a reference for a single segment, but relative to each other for a group of segments. The relative errors between segments in piston, tip, and tilt are measured by the edge sensors. Two approaches can be distinguished: a) all edge sensor measurements used for calculation of the desired position of segments b) only local measurements are used to close the loop for each segment.
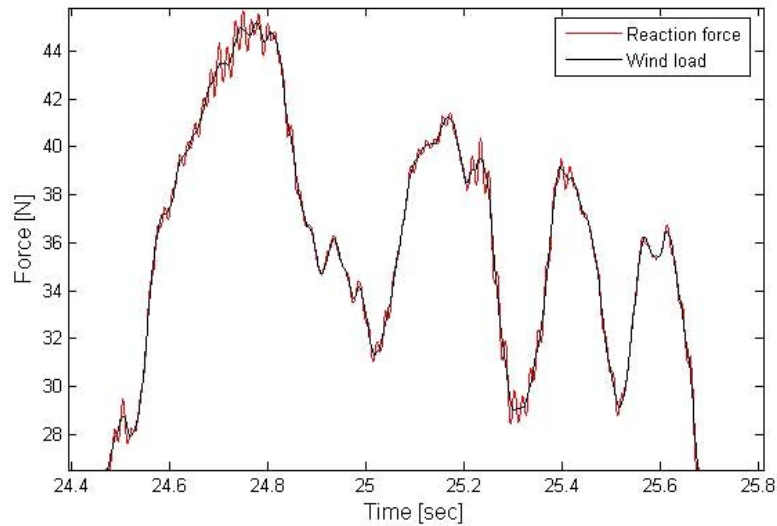
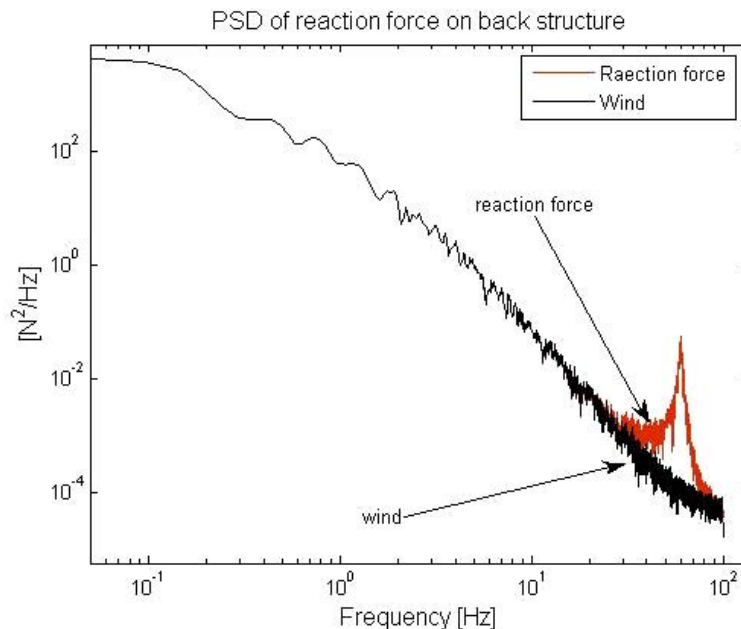*Figure 7-49 Reaction force on back structure and wind load on segment*

Figure 7-50 PSD of wind load and reaction force and back structure

a) Using the interaction matrix[63] these errors can be translated to relative displacements of the segment actuators. These error signals are then fed back to the corresponding segment controller. All sensor readings are used for the construction of the control matrix which is the

---

[63]A matrix defining the geometric relationship between the measurements of the edge sensor and the corresponding relative movements of the actuators.

pseudo-inverse of the interaction matrix. A large optical telescope such as OWL with thousands of sensors in the primary and secondary mirrors requires the manipulation of large matrices resulting in a high and unnecessary computational burden. In addition, when all sensor readings are used for the reconstruction, the noise in the sensors is propagated by the control matrix. The overall noise multiplier scales as the square root of the number of segments [89] and may produce problems as the number of segments increases.

b) To reduce the computational effort and the noise propagation several approaches relying on sparse-matrix operations have been proposed. Local control algorithms relying on measurements over restricted areas can be a good alternative solution. In [90] an approach combining local and global estimators in a hierarchical structure has been proposed. As an alternative approach, a local iterative algorithm using local sensor readings combined with prior state estimates has been proposed in the same paper.

Here a control approach where each segment uses the measurements from edge sensors on the segments has been studied (see RD19). Combinations of the readings from the sensors around one segment, as for example the average error, are directly fed back to the local controller.

The approach has been applied to a ring of seven segments. The dynamical model of the system is described in RD20. Figure 7-51 shows the locations and the numbering of the actuators and the sensors. The only coupling existing in the system is generated by the measurements of the edge sensors.
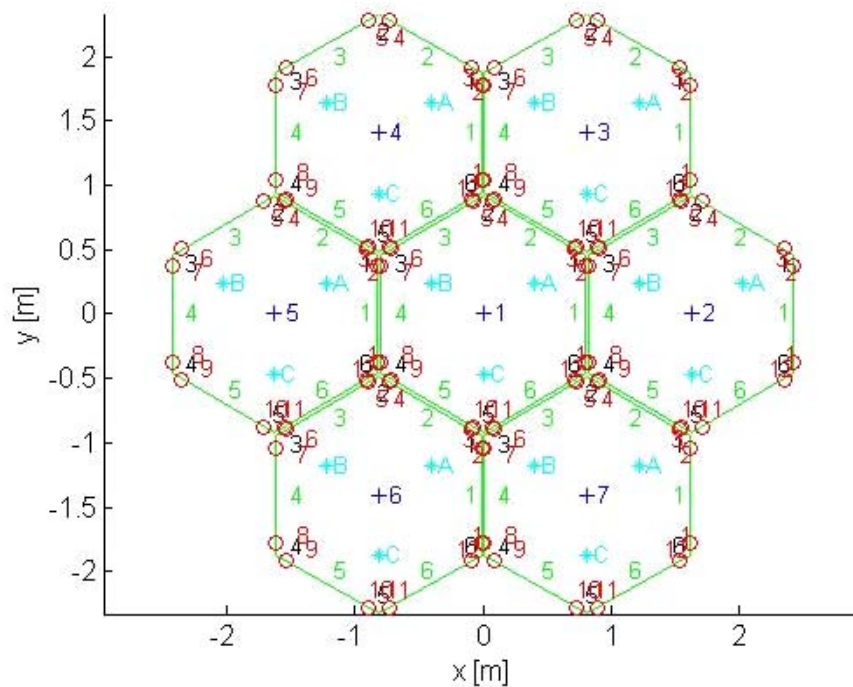

Figure 7-51 Seven segment configuration

Each segment has been subjected to wind perturbations (piston load only) with a mean velocity of 10 m/s. The wind is characterized by a von Karman-type PSD taking into account the correlations between the pressures on different segments. A typical time series of the wind force time is shown in Figure 7-52.
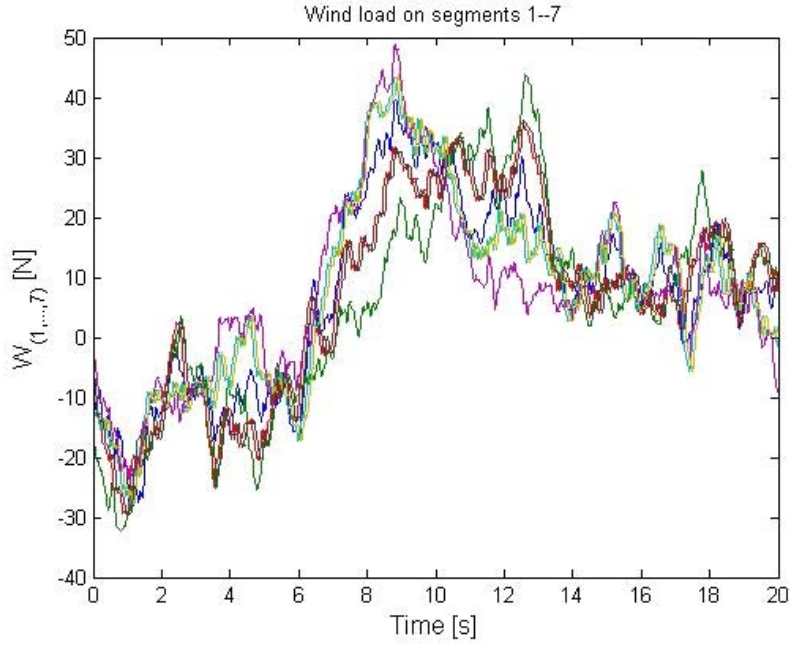
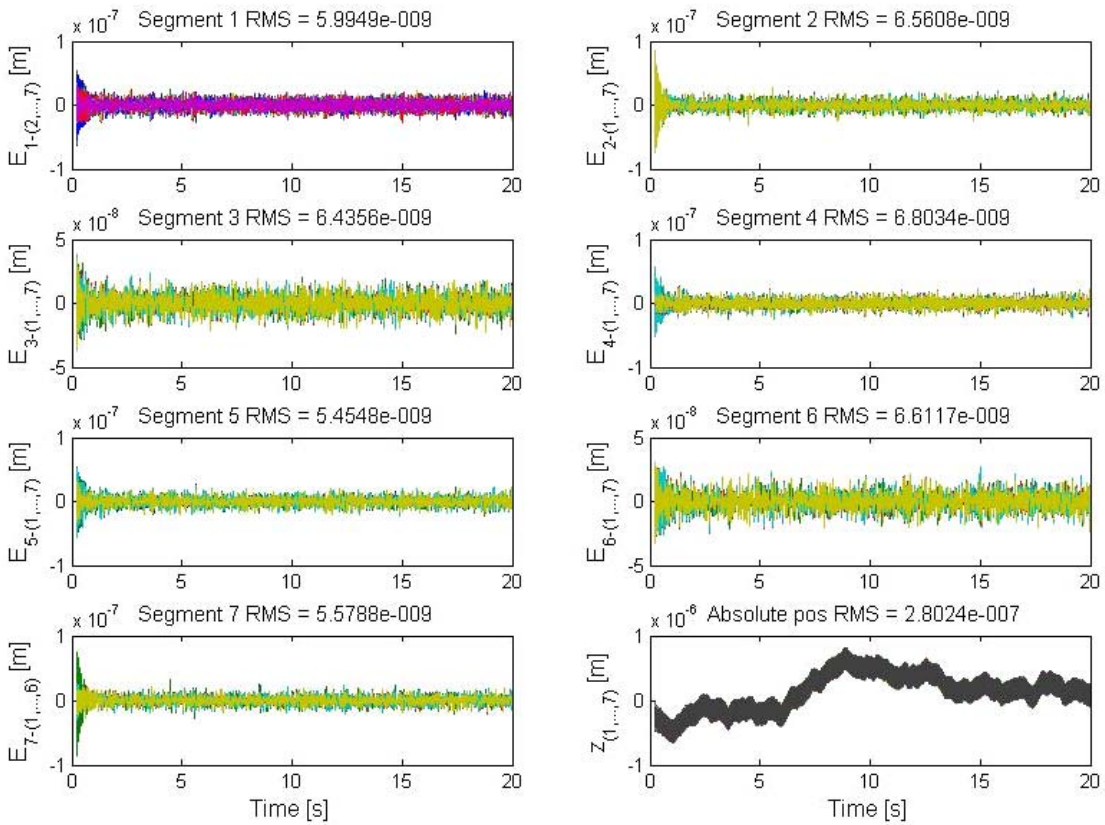*Figure 7-52 Wind load force on seven segments*

Figure 7-53 Seven segment closed-loop simulation: edge sensor readings and absolute position of the segments.

A band-limited white noise with an amplitude of the spectral density of 0.7 nm/$\sqrt{Hz}$ has been injected at the outputs of the edge sensors. The local controller is the one designed for a single segment piston control, i.e. with 10 Hz bandwidth for each actuator and no AFC control. The results of this simulation are shown in Figure 7-53. The RMS errors of all sensor readings are about 6 nm. All segments are moving together while the edge errors are minimized. As expected the absolute positions of the segments represented by the global piston mode are not controlled. It is well known from the modal analysis that four modes, three global rigid body motions and the change of curvature, are undetectable with edge sensors measuring piston steps only [89]. The system has also been simulated using the classical approach with the control matrix. For the few number of segments the results are quite similar and therefore do not allow for a comparison of the two approaches. However, it seems that for a large number of segments the local approach presented here will not suffer from the noise propagation and computational problems associated with the global approach. However, this should be verified later when a system with a larger number of segments will be simulated. This issue as well as the stability proofs related to the local approach are under investigation.

7.6   Active Phasing Experiment (APE)

The Active Phasing Experiment is part of the ELT Design Study and is briefly presented in appendix A-1.2. As explained in that section, the essential purpose of the APE experiment is to explore, integrate, and validate active, that is low temporal frequency, wavefront control schemes and technologies for an Extremely Large Optical Telescope. This includes the evaluation and comparison of the performance of different types of wavefront sensors in the laboratory and on the sky on the one hand and the integration of the control of a segmented aperture control into an already existing active system (including field stabilization and active optics) and driving both the active system and the control of the segments from the output of the full system on the other hand.

To accomplish those tasks APE will be designed as a technical prototype which will be installed and tested at a Nasmyth focus of a VLT Unit Telescope (UT). The telescope provides all active functions (field stabilization, focusing, centering, active deformable mirrors) and the APE instrument emulates the optical effects of segmentation. The latter is done within APE by reimaging the telescope pupil onto a small Active Segmented Mirror (ASM) whose shape is measured by an Internal Metrology (IM). The ASM is composed of 61 hexagonal segments and its inner aperture has a diameter of approximately 130 mm. Each segment is controlled in piston, tip and tilt by 3 piezoelectric actuators. The final wavefront is measured by three new types of Phasing Wave Front Sensors (PWFSs) and a Shack-HArtmann Phasing Sensor (SHAPS) combined in the Phasing Metrology Module. The new types of PWFSs are a phase filtering sensor called ZErnike Unit for Segment phasing (ZEUS), the DIffraction Image Phase Sensing Instrument (DIPSI) evolved from a curvature sensor, and a PYramid Phasing Sensor (PYPS). SHAPS is used for reference and comparison of the measurements of the phase errors at segment edges. SHAPS is also equipped with a lenslet array for the detection of the aberrations of the telescope to be corrected by active optics. The block diagram of this experiment is shown in appendix A-1.2.

7.6.1   Opto-mechanical design

The Active Phasing Experiment will be installed on a 3 m by 2 m optical table. This table will be placed at a height of 90 cm in the laboratory and at the height of the optical axis above the Nasmyth platform of the UT (2 m) as shown in Figure 7-54.
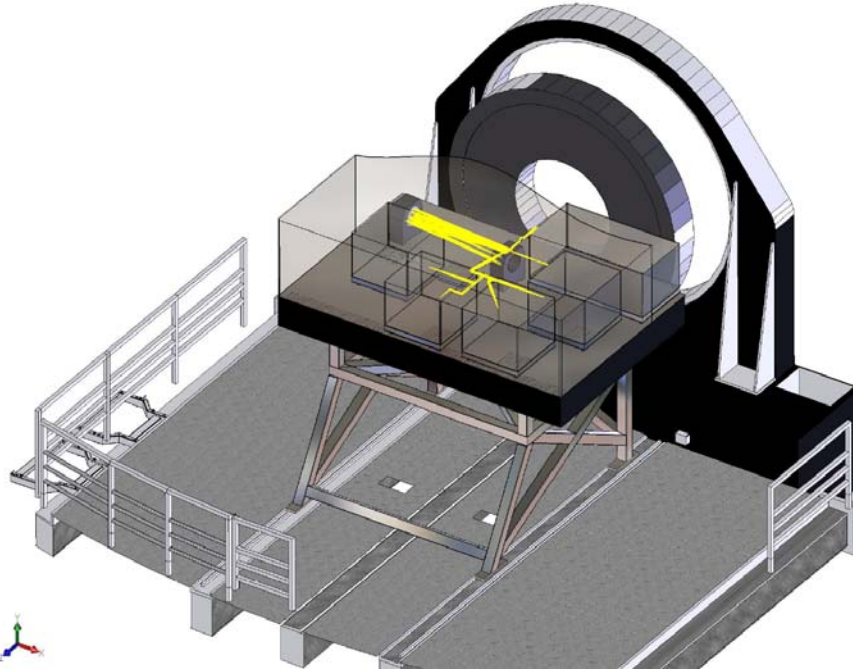
Figure 7-54: 3D view APE on the nasmyth platform

The plane defined by the optical axis on the APE experiment is 230 mm above the optical table. The major components of the optical design of APE are shown in appendix A-1.2. After a derotation of the beam from the telescope an off-axis parabola forms an image of the telescope pupil on the Active Segmented Mirror. The light selected by the field selector is then divided by a beam splitter. 20% of the light is sent to two cameras. One is a guiding camera for the control of the image position in the focal plane. The other one is an imaging camera which is used for the selection of a star for the wavefront sensors and for a direct measurement of the quality of the final images obtained after a correction of the telescope optics and the Active Segmented Mirror. The remaining 80% of the light is sent to the Phasing Wavefront Sensor module, where it is equally distributed among four different phasing wavefront sensors.

The Active Segmented Mirror is composed of 61 hexagonal segments. Its inner diameter is 130 mm, which exceeds the diameter of the image of the telescope pupil. Figure 7-55 shows a 3D view of the ASM. Each segment can be positioned by 3 piezoelectric actuators in piston, tip and tilt with a displacement range of 15 microns.
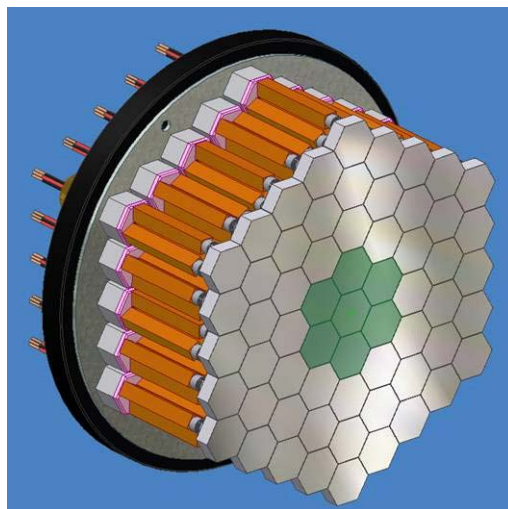

Figure 7-55: 3D view of the ASM

Non-adaptive wavefront control

7.6.2 Internal Metrology

The ASM is controlled by an Internal Metrology system (IM). This device is based on a Twyman-Green interferometer. It uses a synthetic wavelength generated by 2 wavelengths to obtain a measurement range of more than 15 microns. Figure 7-56 shows the conceptual design of the Internal Metrology.
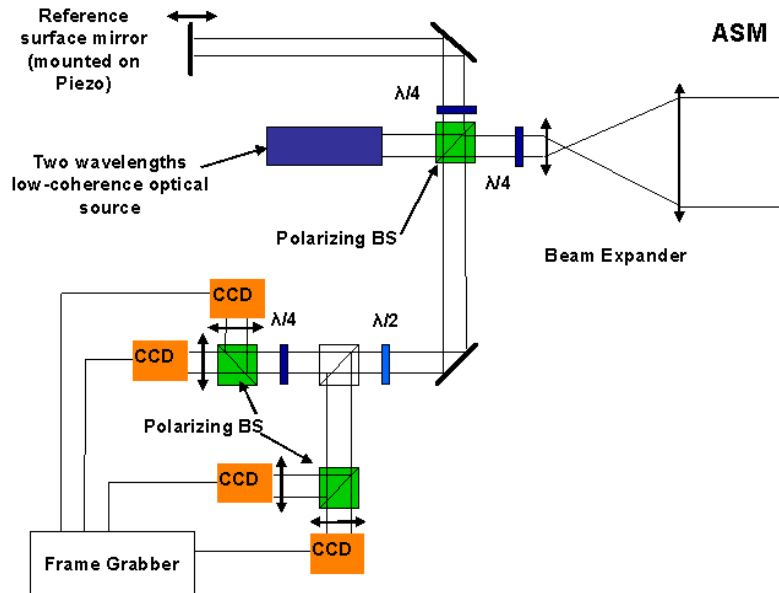
Figure 7-56: Conceptual design of the IM

The measurement frequency is 10 Hz. Apart from delivering the signals for the control of the Active Segmented Mirror it will also check the quality of the correction of the ASM based on the signals from the four phasing wavefront sensors.

7.6.3 The Phasing WaveFront Sensor Module

The PWFS module is composed of 4 different sensors which are based on four different technologies. They are: the Diffraction Image Phase Sensing Instrument (DIPSI) developed by the Instituto de Astrofisica de Canarias (IAC), the Zernike Unit for Segment phasing (ZEUS) developed by the Laboratoire d'Astrophysique de Marseille (LAM) in France, The Pyramid Phasing Sensor (PYPS) developed by INAF and the Shack-Hartmann Phasing Sensor (SHAPS) developed by ESO. DIPSI is based on curvature sensing explained in sect. 7.5.4.2.4 ZEUS on phase filtering explained in sect.. 7.5.4.2.2, PYPS on the pyramid sensing technique explained in sect.. 7.5.4.2.5, and finally SHAPS on the well known Shack Hartmann sensor explained in sect. 7.5.4.2.1.

The four sensors can be tested simultaneously under identical environmental conditions (temperature, humidity, wind speed and seeing) and with identical detectors. This offers the possibility to compare and quantify the capabilities of the four techniques applied to the measurement of phasing wavefront errors.

7.6.4 Schedule and observations

The design review of APE is planned for November 2005. The integration shall start during the second quarter of 2006 and the laboratory test will be performed during the last quarter of 2006. Two periods of one week each of test on the sky on one of the unit telescopes of the VLT on Paranal are planned for 2007.

Non-adaptive wavefront control